SpinFlowSim: A blood flow simulation framework for histology-informed diffusion MRI microvasculature mapping in cancer

Anna Kira Voronova [a,b] , Athanasios Grigoriou [a,b] , Kinga Bernatowicz [a] , Sara Simonetti [a],
Garazi Serna [a] , Núria Roson [c,d] , Manuel Escobar [c,d] , Maria Vieito [e] , Paolo Nuciforo [a],
Rodrigo Toledo [a] , Elena Garralda [e] , Els Fieremans [f] , Dmitry S. Novikov [f] , Marco Palombo [g,h] ,
Raquel Perez-Lopez [a],*,[1] , Francesco Grussu [a],*,[1]

[a] *Vall d'Hebron Institute of Oncology (VHIO), Vall d'Hebron Barcelona Hospital Campus, Barcelona, Spain*
[b] *Department of Biomedicine, Faculty of Medicine and Health Sciences, University of Barcelona, Barcelona, Spain*
[c] *Institut de Diagnòstic per la Imatge (IDI), Barcelona, Spain*
[d] *Department of Radiology, Hospital Universitari Vall d'Hebron, Barcelona, Spain*
[e] *Medical Oncology Service, Vall d'Hebron Barcelona Hospital Campus, Vall d'Hebron Institute of Oncology (VHIO), Barcelona, Spain*
[f] *Bernard and Irene Schwartz Center for Biomedical Imaging, Department of Radiology, New York University Grossman School of Medicine, New York, NY, USA*
[g] *Cardiff University Brain Research Imaging Centre (CUBRIC), School of Psychology, Cardiff University, Cardiff CF24 4HQ, United Kingdom*
[h] *School of Computer Science and Informatics, Cardiff University, Cardiff, United Kingdom*

ARTICLE INFO

ABSTRACT

Diffusion Magnetic Resonance Imaging (dMRI) sensitises the MRI signal to spin motion. This includes Brownian diffusion, but also flow across intricate networks of capillaries. This effect, the intra-voxel incoherent motion (IVIM), enables microvasculature characterisation with dMRI, through metrics such as the vascular signal fraction f_V or the vascular Apparent Diffusion Coefficient (ADC) D^*. The IVIM metrics, while sensitive to perfusion, are protocol-dependent, and their interpretation can change depending on the flow regime spins experience during the dMRI measurements (e.g., diffusive vs ballistic), which is in general not known for a given voxel. These facts hamper their practical clinical utility, and innovative vascular dMRI models are needed to enable the *in vivo* calculation of biologically meaningful markers of capillary flow. These could have relevant applications in cancer, as in the assessment of the response to anti-angiogenic therapies targeting tumour vessels. This paper tackles this need by introducing *SpinFlowSim*, an open-source simulator of dMRI signals arising from blood flow within pipe networks. SpinFlowSim, tailored for the laminar flow patterns within capillaries, enables the synthesis of highly-realistic microvascular dMRI signals, given networks reconstructed from histology. We showcase the simulator by generating synthetic signals for 15 networks, reconstructed from liver biopsies, and containing cancerous and non-cancerous tissue. Signals exhibit complex, non-mono-exponential behaviours, consistent with *in vivo* signal patterns, and pointing towards the co-existence of different flow regimes within the same network, as well as diffusion time dependence. We also demonstrate the potential utility of SpinFlowSim by devising a strategy for microvascular property mapping informed by the synthetic signals, and focussing on the quantification of blood velocity distribution moments and of an *apparent network branching* index. These were estimated *in silico* and *in vivo*, in healthy volunteers scanned at 1.5T and 3T and in 13 cancer patients, scanned at 1.5T. In conclusion, realistic flow simulations, as those enabled by *SpinFlowSim*, may play a key role in the development of the next-generation of dMRI methods for microvascular mapping, with immediate applications in oncology.

1. Introduction

In diffusion Magnetic Resonance Imaging (dMRI), water proton motion is encoded in the acquired signals through magnetic field gradients (Kiselev, 2017). Diffusion encoding provides sensitivity not only to Brownian motion due to pure diffusion, but also to pseudo-diffusion effects arising from the incoherent flow of blood protons through intricate capillary networks (Le Bihan et al., 1986). Flow

---

through sets of pseudo-randomly distributed capillaries leads to magnitude dMRI signal attenuation, a phenomenon known as Intra-Voxel Incoherent Motion (IVIM) effect. IVIM enables the *in vivo* characterisation of microvascular perfusion through dMRI (Le Bihan, 2019), relevant in a variety of diseases, as, for example, in cancer (Fokkinga et al., 2024). Cancers feature aberrant microvasculature, whose flow patterns can differ considerably from normal tissues (Munn, 2003). Tumour vasculature is targeted specifically by anti-angiogenic treatments, which are being used in several cancers (e.g., in liver or kidney carcinomas (Jayson et al., 2016)) and tested in combination with therapies such as immune check-point inhibitors, with promising results (Huinen et al., 2021). The non-invasive assessment of vascular properties through dMRI can equip physicians with new tools for tumour characterisation and longitudinal assessment. It is thereby an active field of research, with studies spanning from malignancy detection to treatment response assessment (Iima et al., 2018; Perucho et al., 2021).

IVIM methods typically rely on disentangling vascular from extravascular tissue dMRI signals (Barbieri et al., 2016b,a). Multi-exponential models are routinely used for this purpose, providing metrics such as the vascular signal fraction f_v, or the *pseudo-diffusion* (vascular) apparent diffusion coefficient (ADC) D^*, whose estimation has been recently made more robust by deep learning (Barbieri et al., 2020; Zheng et al., 2023). Both f_v and D^* are useful indices, as they have shown value in cancer assessment (Dappa et al., 2017). However, these metrics have limitations, since they entangle several, different microvascular characteristics into a single number, e.g., the product between the mean of the blood velocity and capillary length distributions in the diffusive flow regime (Le Bihan and Turner, 1992-09). Moreover, they do not account for higher-order cumulants of the diffusion decay (e.g., kurtosis terms proportional to b^2), and their actual numerical value can depend on the acquisition protocol in non-trivial ways (Wu and Zhang, 2019). In practice, this makes routine IVIM metrics semi-quantitative, surrogate parameters, a fact that, together with their known high variability (Barbieri et al., 2020), hampers their large-scale clinical deployment.

Recently, the numerical simulation of dMRI signals within histologically-realistic voxel models is being increasingly used to inform parameter estimation (Nilsson et al., 2010; Nguyen et al., 2014; Fieremans and Lee, 2018; Buizza et al., 2021; Morelli et al., 2023). Simulation-informed approaches increase the realism of signal models, and may thus improve the biological fidelity of dMRI parametric maps (Nedjati-Gilani et al., 2017; Palombo et al., 2019). However, up to date dMRI simulations have been dominated by Monte Carlo Brownian random walks (Hall and Alexander, 2009; Ginsburger et al., 2019; Rafael-Patino et al., 2020; Lee et al., 2021). Given that only a few simulation frameworks have focussed on blood flow (Van et al., 2021; Weine et al., 2024), there is an urgent need for new, histologically-meaningful, and reproducible simulators tailored for dMRI signal arising from blood flow. These could be used to inform novel numerical approaches for non-invasive microvasculature mapping based on dMRI, which could equip oncologists with biologically-meaningful vascular markers in clinical settings. The new dMRI methods could enable the characterisation of capillary flow patterns that are not captured by classical IVIM f_v and D^*, e.g., informing on anisotropic flow patterns, higher-order cumulants or diffusion-time dependence of the vascular signal.

With this article we aim to fill this scientific gap. We present an open-source framework for blood flow simulation within vascular networks, referred to as *SpinFlowSim* from here on, and demonstrate its potential to inform microvasculature property estimation in dMRI. We start by illustrating the computational engine behind SpinFlowSim, based on pipe network theory. Afterwards, we describe the synthesis of dMRI signals arising from flow within realistic vascular networks obtained from histological images of human tumours. Finally, we showcase a potential application of SpinFlowSim, by using the synthetic signals to inform microvasculature property estimation, which is

demonstrated *in silico* and *in vivo*, in healthy volunteers and in cancer patients. Preliminary findings were disseminated at a conference in abstract form (Voronova et al., 2024b). A draft of this article has also been posted as in the *medRxiv* preprint server (Voronova et al., 2024a).

2. Methods

In this section we illustrate the computational engine upon which SpinFlowSim relies, illustrated in Fig. 1. Afterwards, we present the histological data used to generate realistic vascular networks, and then describe how synthetic dMRI signals were used to inform microvasculature parameter estimation *in silico* and *in vivo*. SpinFlowSim is made freely available at https://github.com/radiomicsgroup/SpinFlowSim.

2.1. Simulation framework

In SpinFlowSim (Fig. 1) we aim to reconstruct the distribution of volumetric flow rate (VFR) across the different segments of an input vascular network. The following characteristics of the vascular network are specified directly by the user:

- a list of capillary segments with their radii;
- the 3D coordinates of the extremities of each segment, referred to as *nodes*;
- the inlet/outlet of the whole network;
- the input VFR q_{in}.

To obtain the VFR distribution, we solve a linear inverse problem, in which the pressure drop $\Delta p_{k,n}$ across each pair of connected nodes (k, n) is proportional to the VFR $q_{k,n}$ between k and n through a flow resistance coefficient $R_{k,n}$, via

$$\Delta p_{k,n} = R_{k,n} q_{k,n}. \tag{1}$$

The approach, valid for the laminar flow regime in micro-capillaries, has been recently proposed for capillary flow simulations (Schmid et al., 2015; Van et al., 2021).

To solve for all unknown $q_{k,n}$ in Eq. (1), we rely on *PySpice* (Salvaire, 2023), a python package for electric circuit analysis, given that solving our flow problem is formally equivalent to solving a passive electric circuit (electric-hydraulic analogy). Note that in a passive electric circuit, the voltage drop across a resistor is proportional to the product of the electric current through the resistor and the resistance of the element itself, i.e., it is formally equivalent to Eq. (1). In this first demonstration of SpinFlowSim, we compute the resistance between nodes k and n through a modified Hagen–Poiseuille law, as done in Blinder et al. (2013):

$$R_{k,n} = 4 \left(1 - 0.863\, e^{-\frac{r_{k,n}}{14.3\mu m}} + 27.5\, e^{-\frac{r_{k,n}}{0.351\mu m}} \right) \frac{8\, \mu\, L_{k,n}}{\pi\, r_{k,n}^4}. \tag{2}$$

Eq. (2) models the effect of the hematocrit as well as erythrocyte-capillary wall interactions (Pries and Secomb, 2008; Blinder et al., 2013). Above, μ is the dynamic viscosity of pure plasma (Késmárky et al., 2008) ($\mu = 1.20$ mPa s at 37 °C), $r_{k,n}$ is the radius of the capillary segment, and $L_{k,n}$ its length.

After recovering the VFR $q_{k,n}$ between each pair of connected nodes, in SpinFlowSim we obtain the corresponding mean velocity $v_{k,n}$ as

$$v_{k,n} = \frac{q_{k,n}}{\pi r_{k,n}^2}. \tag{3}$$

Finally, the 3D trajectory $\mathbf{p}_w(t)$ of the generic w-th blood spin is synthesised by integrating the discrete-time system

$$\mathbf{p}_w(t + \Delta t) = \mathbf{p}_w(t) + \Delta t\, v_w(t)\, \mathbf{n}_w(t) \tag{4}$$

given an initial position $\mathbf{p}_w(0) = \mathbf{p}_{w,0}$. In Eq. (4), Δt is the temporal resolution of the simulation, while $v_w(t)$ and $\mathbf{n}_w(t)$ are the instantaneous velocity vector magnitude and direction experienced by the spin at time t. Spins' initial positions $\mathbf{p}_{w,0}$ are seeded across the whole network, with
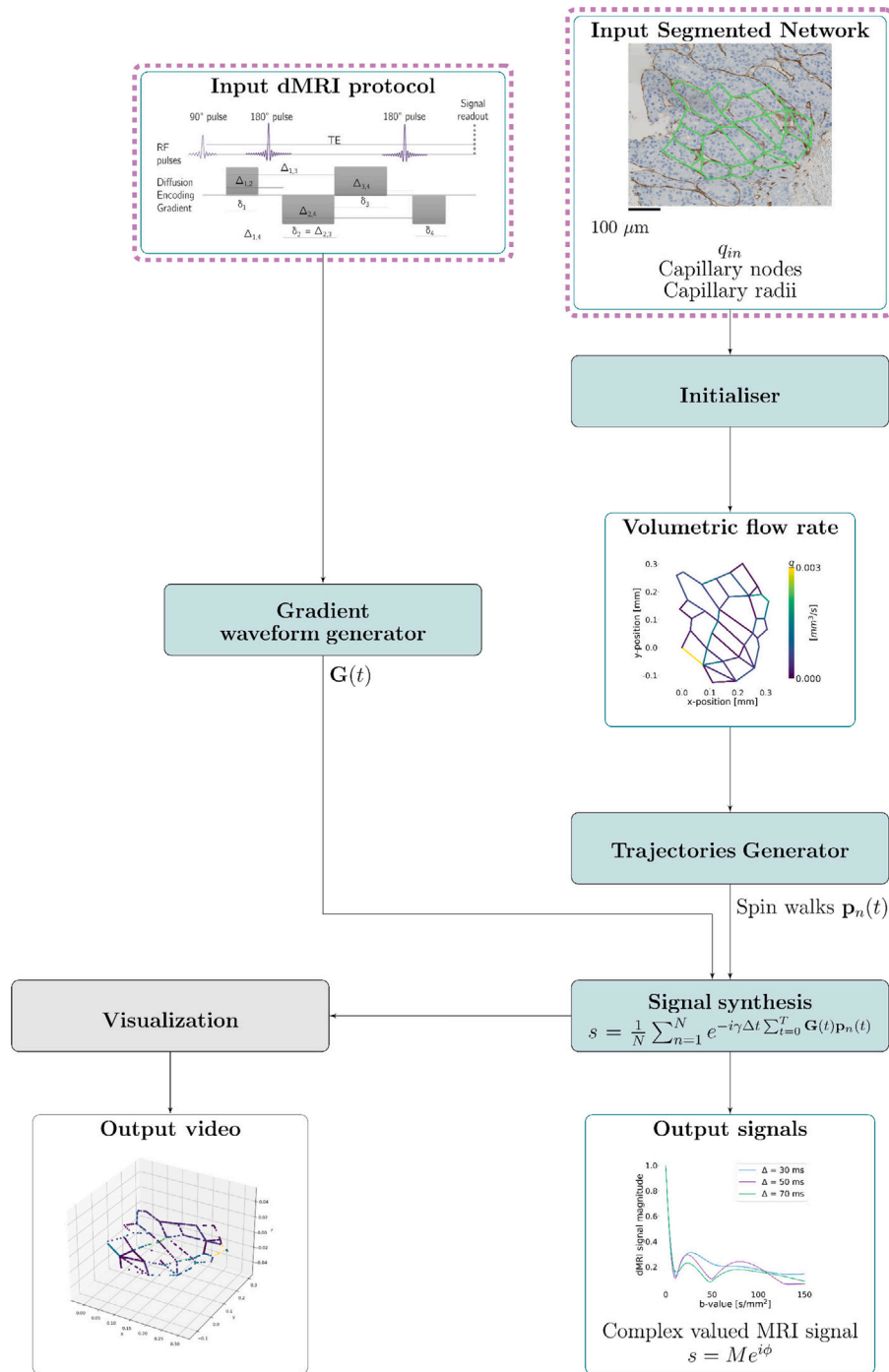
Fig. 1. Outline of the proposed SpinFlowSim framework. The dashed boxes indicate user-provided input information. An illustrative example of a network segmented on a biopsy with resolved volumetric flow rates for an input flow $q_{in} = 3.1 \cdot 10^{-3}$ mm^3/s and synthesised signals are shown.

uniform spin density in each segment. The numbers of spins assigned to each segment is proportional to its volume (Van et al., 2021). During the integration of Eq. (4), spins reaching the termination of a capillary are assigned at random to one of the emanating branches. The probability of a spin being assigned to a specific branch is proportional to the VFR through that branch (Van et al., 2021). More formally, once a flowing spin reaches the k-th node, the probability of it continuing its trajectory in the $k \rightarrow n$ branch emanating from k is

$$p(k \rightarrow n) = \frac{q_{k,n}}{\sum_n q_{k,n}}. \qquad (5)$$

Moreover, spins reaching the network outlet continue flowing through a shifted copy of the vascular network, whose inlet position coincides

exactly with the outlet itself. This ensures that no spins are lost during the simulation (periodic boundary condition). SpinFlowSim supports the visualisation of spin trajectories as a video, in order to facilitate the visual inspection of the simulation output.

Once the trajectories for W spins have been generated, we synthesise a complex-valued dMRI signal s for any input gradient wave form $\mathbf{G}(t)$ as (Fieremans and Lee, 2018)

$$s = \frac{1}{W} \sum_{w=1}^{W} e^{-i \gamma \Delta t \sum_{t=0}^{T} \mathbf{p}_w(t) \cdot \mathbf{G}(t)} \qquad (6)$$
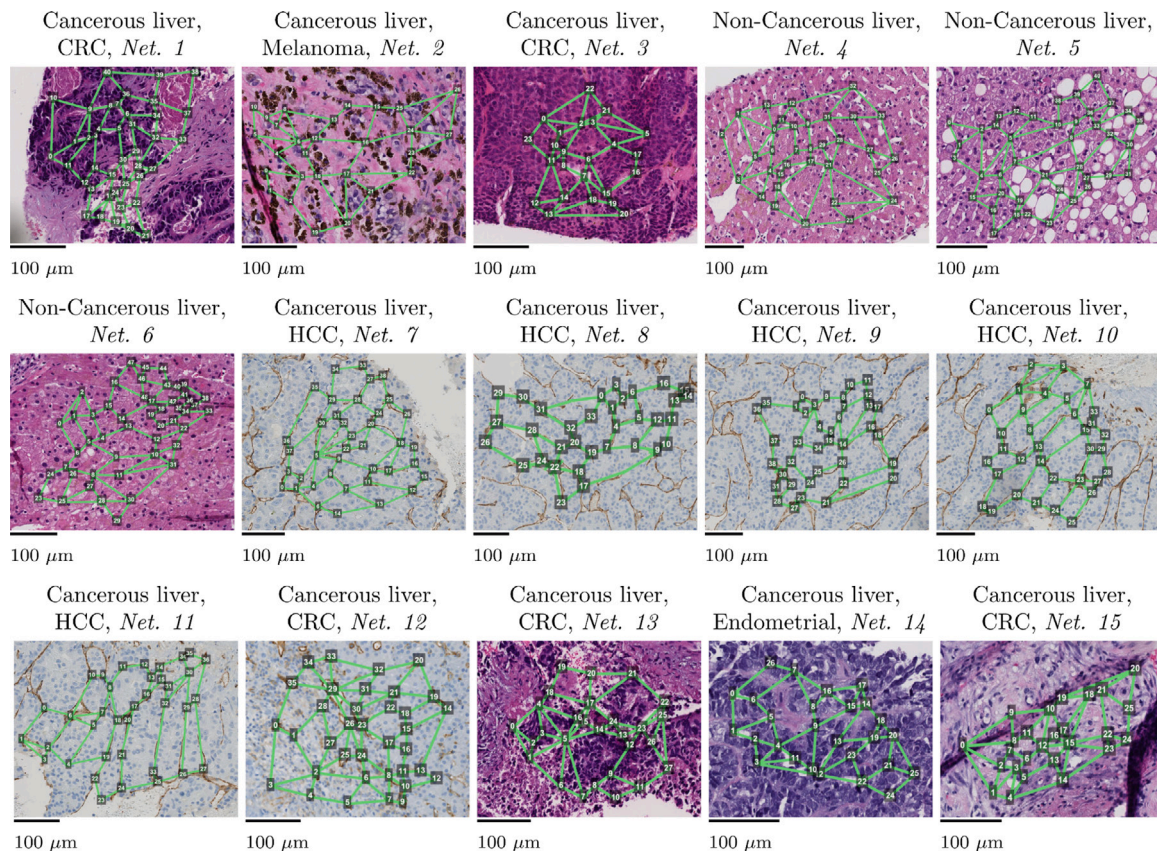
given the requested total simulation duration T.

Fig. 2. Vascular networks segmented on digitised liver tumour biopsies (resolution: 0.454 µm). Each network is labelled as "Non-Cancerous" or "Cancerous", depending on whether it was drawn on non-cancerous liver parenchyma or on tumour tissue. For the latter case, the primary cancer is also indicated (CRC stands for Colorectal Cancer, while HCC for Hepatocellular Carcinoma). The non-cancerous networks were drawn on liver tissue found on liver tumour biopsies of patients suffering from Melanoma (n = 2) and Ovarian cancer (n = 1).
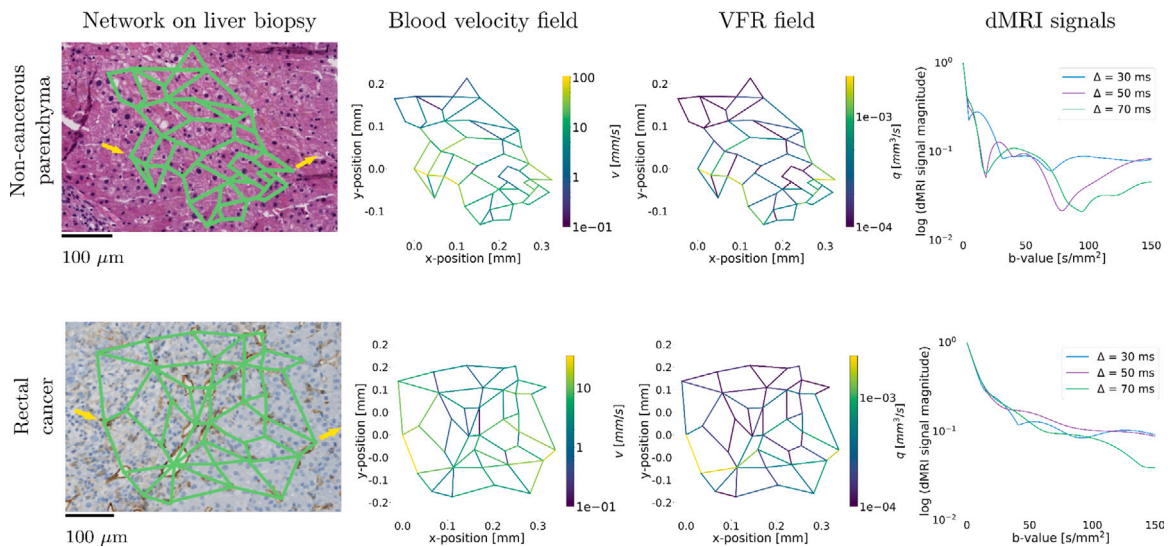

Fig. 3. Examples of resolved vascular networks. The top row shows results from a vascular network segmented on a HE-stained non-cancerous liver region, found on a biopsy of a patient with metastatic melanoma (Net 6). The bottom panel shows results from a CD31-stained rectal cancer area (Net 12). From left to right, we show the vascular network, the resolved blood flow velocity field for $q_{in} = 3.1 \cdot 10^{-3}$ mm^3/s, and examples of dMRI signal decay over a range of b-values (0–150 s/mm^2) and diffusion times ($\Delta = \{30, 50, 70\}$ ms, $\delta = 20$ ms). The inlet/outlet were: nodes 0 and 33 for Net 6; nodes 0 and 14 for Net 12. These have been indicated by input/output yellow arrows.
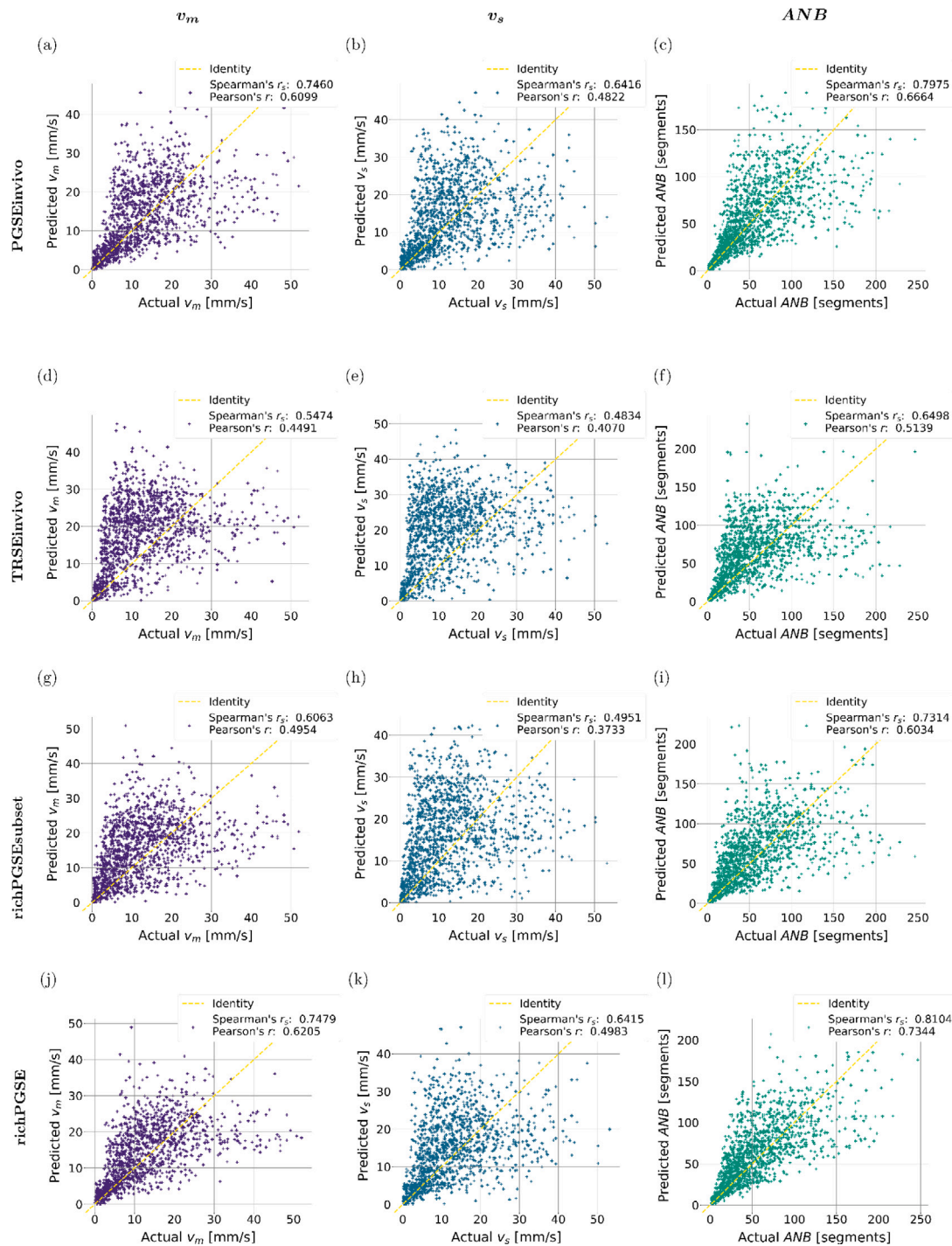
Fig. 4. Scatter plots relating estimated and ground truth microvascular parameters in computer simulations. First row (panels (a), (b), (c)): results for protocol "PGSE in vivo". Second row (panels (d), (e), (f)): results for protocol "TRSE". Third row (panels (g), (h), (i)): results for protocol "richPGSE subset". Fourth row (panels (j), (k), (l)): results for protocol "richPGSE". From left to right: results for metric v_m (panels (a), (d), (g), (j)); results for metric v_s (panels (b), (e), (h), (k)); results for metric ANB (panels (c), (f), (i), (l)).Spearman's and Pearson's correlation coefficients between estimated and ground truth values are also reported in each plot.

2.2. Vascular networks

We deployed SpinFlowSim on vascular networks reconstructed from 2D histological images. These consisted of biopsies obtained in patients suffering from advanced tumours and participating in an ongoing imaging study at the Vall d'Hebron Institute of Oncology (Barcelona).

The biopsied tissue, taken from liver tumours, was processed and stained. Digitised images of the stained tissue were acquired on a Hamamatsu C9600-12 optical slide scanner (resolution: 0.454 µm). For

this study, we used 11 histological images, obtained from 11 patients. For each patient, we had access to either a routine hematoxylin-eosin (HE) stain (n = 9) or a CD31 stain (n = 2).

We drew a total of 15 2D networks. We drew networks manually, by tracing visible capillaries in non-cancerous liver parenchyma or in cancerous regions-of-interest (ROIs). Networks were drawn on approximately square ROIs, of sizes ranging from 250 to 550 µm per side. Networks were made of interconnected segments, with curved capillaries approximated by a piece-wise series of straight pipes. A
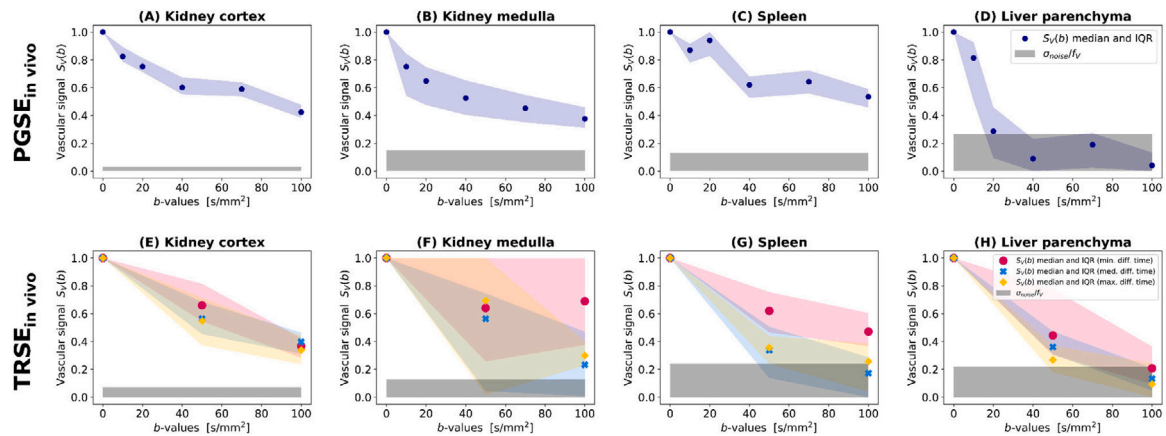
Fig. 5. Representative vascular voxel signals measured in two healthy volunteers *in vivo*. Top (A–D): signals from healthy volunteer 4, scanned on a 3T system, with the "PGSEinvivo" protocol, based on routine PGSE. Bottom (E–H): signals from healthy volunteer 2, scanned on a 1.5T system, with the "TRSEinvivo" protocol, based on a DW TRSE acquisition. From left to right, signals from different ROIs are shown: kidney cortex (A and E); kidney medulla (B and F); spleen (C and G); liver parenchyma (D and H). The figure reports the median and the inter-quartile range of variation of the signal across voxels within the ROI. An estimated range of noise floor fluctuations is also reported in grey.
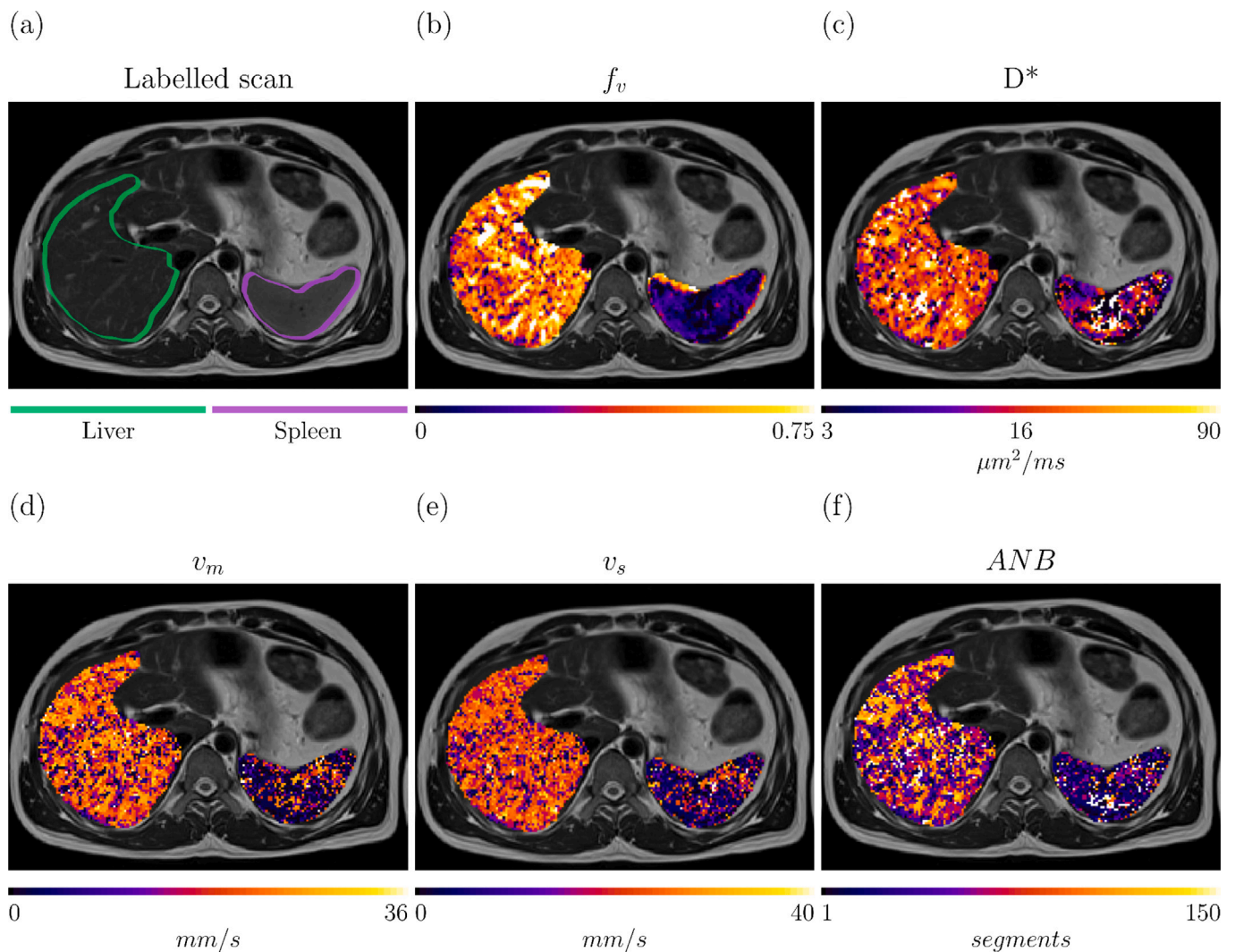

Fig. 6. Microvascular maps in a representative healthy volunteer scanned on the 1.5T system with protocol "TRSEinvivo". (a): labelled scan; (b) and (c): IVIM maps f_V and D^*; (d), (e) and (f): microvascular indices v_m, v_s and ANB. In the labelled scan, we highlight the location of the liver and the spleen.
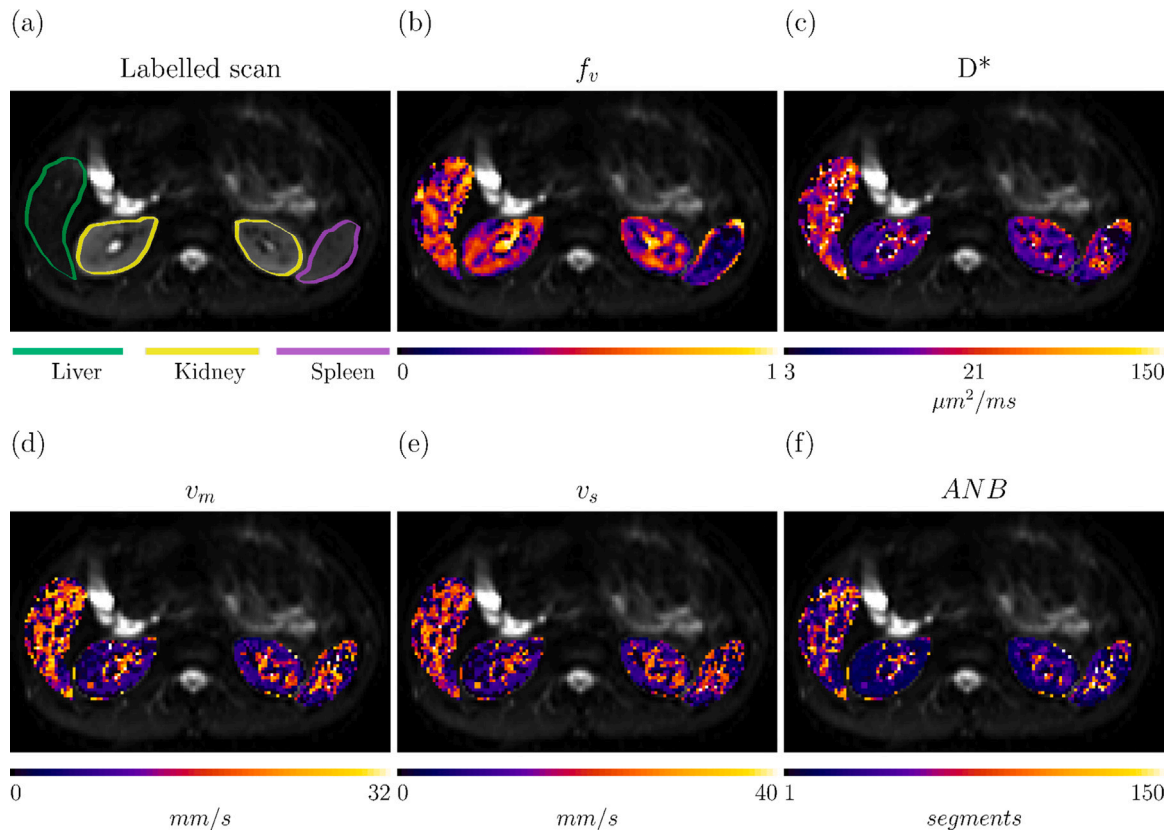
Fig. 7. Microvascular maps in the healthy volunteer scanned on the 3T system with protocol "PGSEinvivo". (a): labelled scan; (b) and (c): IVIM maps f_V and D^*; (d), (e) and (f): microvascular indices v_m, v_s and ANB. In the labelled scan, we highlight the location of the liver, the spleen and of the kidneys.
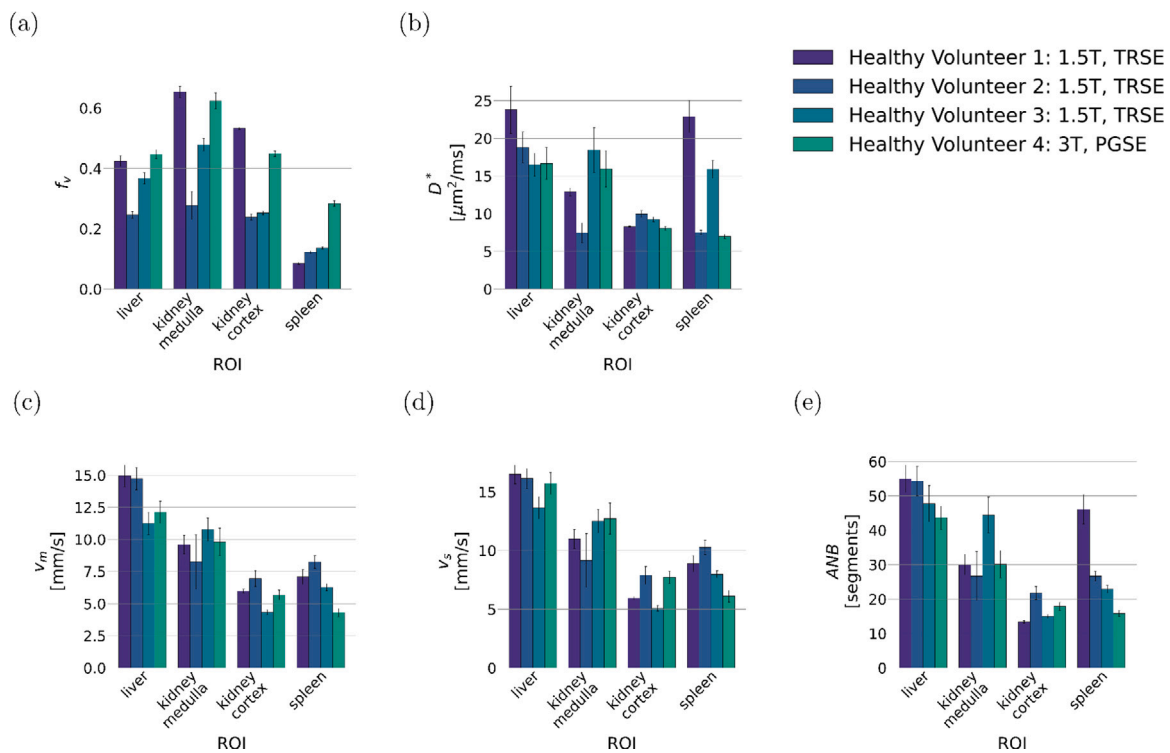

Fig. 8. Bar plots reporting mean and standard error of the mean of all microvascular metrics in the different regions-of-interest (ROIs) of the four healthy volunteers. (a): trends for metric f_V; (b): trends for metric D^*; (c): trends for metric v_m; (d): trends for metric v_s; (e): trends for metric ANB.
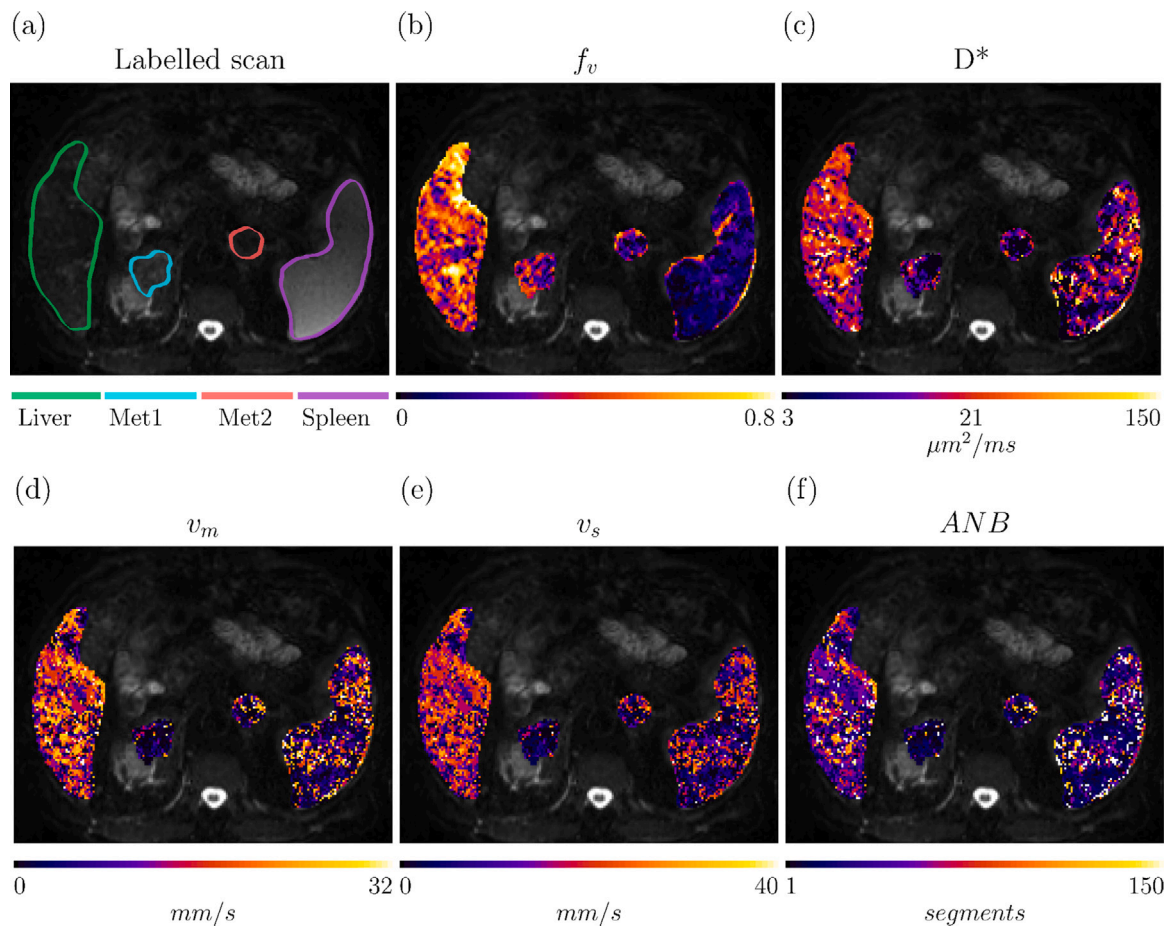
Fig. 9. Parametric maps obtained in adrenal metastases, liver and spleen of a 61 y.o. male patient, suffering from advanced rectal cancer (patient 8, scanned on a 1.5T Siemens Avanto system with a DW TRSE sequence). Top row: labelled scan and IVIM maps f_V and D^*. Bottom row: microvascular parameters obtained via simulation-informed model fitting, namely: mean blood velocity v_m, blood velocity standard deviation v_s, and Apparent Network Branching ANB.

characteristic radius was assigned to each segment by averaging three radius measurements, performed at the inlet, middle point, and outlet level. For each network, we computed an approximated network size as the maximum euclidean distance between any pair of nodes. Additionally, we also assessed the network dimensions by calculating the total number of capillary segments. As compared to the euclidean network size mentioned above, this index has the potential of distinguishing between networks of similar dimensions, but characterised by different spatial densities of capillaries. We also computed the mean and standard deviation of the capillary radii and lengths (r and L), which we refer to as r_m and L_m.

We generated 100 VFR distribution realisations by changing randomly the position of the network inlet/outlet 10 times, and varying the input VFR q_{in} for each inlet/outlet pair (10 uniformly-spaced q_{in} values in $[1.5 \cdot 10^{-4}; 5.5 \cdot 10^{-3}]$ mm^3/s), to cover plausible blood capillary velocities (Ivanov et al., 1981). The total duration and the temporal resolution of the simulations were $T = 100$ ms and $\Delta t = 0.01$ ms. We characterised each realisation by computing: mean and standard deviation of the velocity and VFR distribution across capillary segments (v_m and v_s; q_m and q_s); mean radius (r_m), mean segment length (SL_m) and mean path length (PL_m); number of input/output paths; as well an Apparent Network Branching (ANB index). ANB measures the average number of segments spins travel through during a reference time of 100 ms. Conversely, PL_m is instead obtained as $PL_m = \langle PL \rangle$, where PL indicates the length of the generic input/output flow path, obtained through the cumulative length of the segments contained within a path connecting inlet to outlet, i.e., $PL = \sum_{j \in flow\,path} L_j$. In practice, PL_m reports the average PL over all possible input/output network paths.

Spearman's correlation coefficients among all possible pairs of network metrics were computed. Additionally, we studied the correlation among mean VFR q_p, mean velocity v_p, mean radius r_p and path length PL along all possible input/output paths contained in the networks. For each path, these were computed as $q_p = \langle L\,q \rangle / PL$, $v_p = \langle L\,v \rangle / PL$ and $r_p = \langle L\,r \rangle / PL$. The existence of closed flow loops within the networks was also assessed with the graph theory python package *graph-tools* (Peixoto, 2023).

Finally, we synthesised illustrative dMRI signals for routine pulsed-gradient spin echo (PGSE) sequences. We probed b-values in the range [0; 150] s/mm^2, and varied the gradient separation Δ over two orders of magnitude (from 10 ms to 1 s). Signals were generated for two orthogonal directions within the plane containing the 2D networks, as well as for an increasing number of evenly-spaced directions over the unit circle, up to 64, and their magnitude averaged. The fraction of flowing spins that do not change capillary segment during the simulation was also recorded.

2.3. Microvascular property estimation from dMRI

We also investigated whether the synthetic signals generated with SpinFlowSim can be used to inform microvascular parameter estimation in dMRI. We hypothesised that, for a given dMRI protocol, large dictionaries of synthetic, noise-free signal arrays $\mathbf{S} = \{\mathbf{s}_1, \dots, \mathbf{s}_M\}$, coupled with their corresponding vascular parameter arrays $\mathbf{P} = \{\mathbf{p}_1, \dots, \mathbf{p}_M\}$, can be used to find practical numerical implementations of the forward signal model $\mathbf{p} \mapsto \mathbf{s}(\mathbf{p})$. Numerical implementations of this type could be easily incorporated in standard non-linear least square

(NNLS) fitting, used routinely in dMRI, thus avoiding the need for approximated analytical signal expressions.

In the following sections, we will describe *in silico* analyses performed to investigate the feasibility of simulation-informed fitting. We will then describe experiments performed to demonstrate the approach *in vivo*, based on the acquisition of dMRI scans in healthy volunteers at 1.5T and 3T and cancer patients at 1.5T.

2.3.1. In silico estimation

We used SpinFlowSim to synthesise signals for 4 realistic dMRI protocols, and then analysed such signals to test whether it is possible to estimate v_m, v_s and ANB from noisy measurements. One of the protocols represents a rich, comprehensive pulsed-gradient spin echo (PGSE) acquisition, encompassing several b-values in a measurement regime with high sensitivity to IVIM effects (i.e., b smaller than approximately 100 s/mm^2 Le Bihan, 2019), as well as multiple diffusion times. A second protocol is instead a shorter subset of the rich protocol. Finally, the third and fourth protocols match acquisitions used for *in vivo* imaging. Signals were generated for two orthogonal directions within the plane containing the 2D networks, and their magnitude averaged. In summary, the protocols were:

- a rich PGSE protocol, referred to as "richPGSE". It consisted of a total of 99 measurements, encompassing 9 $b = 0$ and 10 non-zero b-values $b = \{10, 20, 30, 40, 50, 60, 70, 80, 90, 100\}$ s/mm^2, each acquired for 9 unique diffusion times, corresponding to $(\delta, \Delta) = \{10, 20, 30\}$ ms $\times$ $\{30, 50, 70\}$ ms.
- A second PGSE protocol, referred to as "richPGSEsubset". It is a subset of the former, and describes a more realistic acquisition that could be implemented under time pressure. It encompassed 3 $b = 0$ and 6 diffusion-weighted (DW) measurements, namely $b = \{50, 100\}$ for 3 different diffusion times. The gradient duration δ was fixed to 20 ms, while the 3 diffusion times were achieved by varying Δ as $\Delta = \{30, 50, 70\}$ ms.
- A DW twice-refocussed spin echo (TRSE) protocol, referred to simply as "TRSEinvivo". It matches the protocol implemented on a 1.5T Siemens Avanto system *in vivo* (see Section 2.3.2 below). It consisted of 3 non-DW and 6 DW measurements. These were $b = \{50, 100\}$, acquired for 3 diffusion times. The gradient duration of the 4 gradient lobes (Supplementary Fig. 1) for the 3 diffusion times were: $\delta_1 = \{8.9, 13.2, 18.9\}$ ms, $\delta_2 = \{17.6, 19.3, 21.0\}$ ms, $\delta_3 = \{20.4, 24.8, 30.5\}$ ms, $\delta_4 = \{6.0, 7.7, 9.5\}$ ms. The separation between the onset of the gradient lobes (Supplementary Fig. 1) were instead: $\Delta_{1,2} = \{17.4, 21.7, 27.5\}$ ms, $\Delta_{1,4} = \{63.9, 74.2, 87.5\}$ ms.
- Another PGSE protocol, referred to as "PGSEinvivo". It matches the protocol implemented on a 3T GE SIGNA Pioneer system *in vivo* (see Section 2.3.2 below). The protocol included the b-values $b = \{0, 10, 20, 40, 70, 100\}$ s/mm^2, with minimal variations of gradient timings across b-values, i.e., $\delta = \{0, 2.06, 2.57, 3.37, 4.18, 4.82\}$ ms, $\Delta = \{0, 31.34, 31.85, 32.65, 33.47, 34.10\}$ ms.

Briefly, we performed a leave-one-out experiment. For each vascular network in turn, we used noise-free signals from 14 out of 15 substrates to learn the forward signal model $(v_m, v_s, ANB) \mapsto s(v_m, v_s, ANB)$, which we then used for estimating v_m, v_s and ANB on noisy signals for the remaining 15th network (signal-to-noise ratio (SNR) at $b = 0$ of 20). The forward signal model $(v_m, v_s, ANB) \mapsto s(v_m, v_s, ANB)$ was learnt by interpolating the set of paired examples signals/vascular parameters with a radial basis function (RBF) regressor, so that fitting could be performed by embedding $s(v_m, v_s, ANB)$ into standard maximum-likelihood NNLS routines (Panagiotaki et al., 2012). Fitting was performed with the freely-available *mri2micro_dictml.py* tool, part of the *bodymritools* python repository (https://github.com/fragrussu/bodymritools). To characterise fitting performance, we generated scatter plots between ground truth and estimated v_m, v_s and ANB, and

computed corresponding Spearman's correlation coefficients. For each leave-one-out iteration, the 100 realisations of each network obtained by varying inlet/outlet and input VFR were not averaged, but rather used as independent entries in the signal/parameter dictionary used to learn the forward signal model. Similarly, microvascular parameters were estimated from signals from all realisations of the 15th test network, which were processed independently.

2.3.2. In vivo estimation

We also investigated the feasibility of using synthetic signals from SpinFlowSim to inform microvascular property estimation *in vivo*, on both healthy volunteers and cancer patients. All participants were scanned after providing informed written consent, in imaging sessions approved by the Clinical Research Ethics Committee (CEIm) of the Vall d'Hebron University Hospital of Barcelona, Spain (codes: PR(AG)29/2020 and PR(IDI)109/2022).

Healthy volunteers: data and analysis. We scanned four healthy volunteers on two MRI scanners. Volunteers 1 to 3 were scanned on a 1.5T Siemens Avanto system (35 yr old, male; 34 yr old, female; 25 yr old, male), while volunteer 4 (32 yr old, male) on a 3T GE SIGNA Pioneer system. The acquisition included routine anatomical structural imaging and dMRI. For the 1.5T scanner, this consisted of a DW TRSE Echo Planar Imaging (EPI) scan, with salient parameters: resolution of 1.9×1.9 mm^2; slice thickness of 6 mm; $b = \{0, 50, 100, 400, 900, 1200, 1600\}$ s/mm^2, with each b acquired at 3 different diffusion times, with the same diffusion times as the "TRSE" protocol used simulations (see Section 2.3.1 above); TE = $\{93, 105, 120\}$ ms for the short, intermediate, and long diffusion time; TR = 7900 ms; trace DW imaging; NEX = 2; GRAPPA = 2; 6/8 Partial Fourier imaging; BW = 1430 Hz/pixel; acquisition of a $b = 0$ image at the shortest TE with reversed phase encoding. For the 3T scanner instead, this consisted of a standard PGSE EPI scan, with salient parameters: resolution 2.4×2.4 mm^2; slice thickness of 6 mm; $b = \{0, 10, 20, 40, 70, 100, 500, 1000, 1250, 1500\}$ s/mm^2; TE = 75 ms; TR = 12 000 ms; trace DW imaging; NEX = 2; ASSET = 2; BW = 3333 Hz/pixel; respiratory gating.

We denoised scans with MP-PCA (Veraart et al., 2016), mitigated Gibbs ringing (Kellner et al., 2016) and corrected for motion and EPI distortions (Andersson et al., 2003) (the latter step only on the 1.5T data). Subsequently, we normalised the signal acquired at each TE to the $b = 0$ signal level at the same TE, when multiple TE were acquired, and then estimated the vascular signal S_V for $b \leq 100$ s/mm^2 in each voxel (Gurney-Champion et al., 2018; Wang et al., 2021) as

$$S_V = S - S_T. \tag{7}$$

Above, S is the measured signal and S_T is an estimate of the extravascular tissue signal. S_T was computed by extrapolating to $b \leq 100$ s/mm^2 an ADC fit $S_T = S_T(b = 0) e^{-b\,ADC_T}$ performed on signal measurements at $b > 100$ s/mm^2.

Afterwards, we fitted (v_m, v_s, ANB) voxel-by-voxel, using the same fitting procedure employed in *in silico* experiments above, but learning the forward model $\mathbf{P} \mapsto \mathbf{S}(\mathbf{P})$ on all 1500 synthetic signals from all vascular networks (i.e., without averaging signals from different network realisations, but rather stacking them as independent entries of the signal/parameter dictionary). For reference, we also computed more standard IVIM metrics f_V and D^*, by fitting $S_V = S_V(b = 0) e^{-b\,D^*}$ to the vascular signal, with $f_V \approx 1 - \frac{S_T(b=0)}{S(b=0)}$. For the 1.5T data, f_V and D^* were computed on the vascular signal estimates at the shortest TE. Mean, standard errors and standard deviations of v_m, v_s, ANB, f_V and D^* within manually drawn ROIs were computed. The ROIs were placed in the liver, spleen, as well as medulla and cortex of a kidney. The estimated vascular signal was plotted as a function of the b-value in an illustrative healthy volunteer for each scanner.

Table 1

Summary of vascular networks with corresponding microvascular properties generated for this study. The non-cancerous networks were drawn on non-cancerous liver tissue found on biopsies from melanoma (n = 2) and ovarian cancer (n = 1) metastases. Mean patient age was 66.2 years. Male = 5, Female = 6. CRC = colorectal cancer, HCC = hepatocellular carcinoma, EC = Endometrial cancer. Vascular network metrics are: mean and standard deviation of blood velocity, v_m and v_s; mean and standard deviation of the VFR, q_m and q_s; apparent network branching ANB; mean radius r_m; mean segment length SL_m; mean path length PL_m; the number of input/output (I/O) paths and the network dimensions. The dimensions have been indicated by two metrics, namely the actual Network Size (maximum euclidean distance between any pair of nodes), and the total number of segments. For ech metric (beyond those describing the network dimensions), the mean and the standard deviation (in bracket) over the 100 realisations of each network (10 input/output node combinations × 10 input VFRs) are reported.

Network	Description	v_m [mm/s]	v_s [mm/s]	ANB [segments]	r_m [µm]	SL_m [µm]	Network size [mm]	q_m [mm³/s] · 10⁴	q_s [mm³/s] · 10⁴	I/O Paths [paths]	PL_m [µm]	Total segments [segments]
Net. 1	Cancerous liver, CRC	13.76 (8.52)	14.05 (9.69)	46.51 (22.15)	3.1 (0.9)	46.24 (13.95)	0.35	4.25 (2.66)	4.19 (2.56)	376 (313)	382.59 (44.2)	67
Net. 2	Cancerous liver, Melanoma	11.24 (7.01)	13.69 (9.18)	28.33 (13.92)	4.02 (1.37)	60.85 (21.59)	0.39	4.94 (3.07)	4.74 (2.93)	100 (26)	460.78 (26.1)	45
Net. 3	Cancerous live, CRC	24.54 (14.9)	19.76 (12.14)	56.91 (23.3)	2.45 (0.95)	53.19 (21.38)	0.24	4.72 (2.87)	4.27 (2.67)	187 (76)	315.76 (25.2)	42
Net. 4	Non-cancerous liver	4.81 (2.93)	3.81 (2.35)	12.38 (6.42)	5.14 (1.64)	81.54 (27.72)	0.50	3.91 (2.38)	3.39 (2.09)	353 (209)	614.36 (39.1)	60
Net. 5	Non-cancerous liver	10.42 (6.38)	8.16 (5.01)	35.95 (17.13)	3.76 (1.03)	53.03 (15.54)	0.39	4.53 (2.78)	3.69 (2.24)	536 (183)	711.76 (32.7)	65
Net. 6	Non-cancerous liver	10.99 (6.79)	11.05 (6.98)	36.92 (17.55)	3.43 (0.9)	48.23 (13.26)	0.42	4.28 (2.7)	4.47 (2.77)	1432 (927)	752.97 (91.8)	77
Net. 7	Cancerous liver, HCC	10.54 (6.59)	10.24 (6.8)	33.77 (16.18)	3.54 (1.03)	60.12 (17.81)	0.36	4.41 (2.71)	5.09 (3.1)	192 (70)	610.74 (76.8)	60
Net. 8	Cancerous liver, HCC	8.42 (7.68)	12.71 (10.52)	13.74 (6.71)	5.36 (1.78)	70.9 (22.43)	0.60	5.81 (3.97)	7.48 (4.58)	48 (18)	539.79 (62.0)	47
Net. 9	Cancerous liver, HCC	13.92 (9.27)	17.06 (12.41)	32.78 (16.59)	3.7 (1.05)	55.28 (16.45)	0.41	5.23 (3.27)	5.24 (3.24)	42 (9)	430.99 (51.5)	52
Net. 10	Cancerous liver, HCC	8.68 (5.46)	9.8 (6.52)	17.96 (8.71)	4.71 (1.59)	68.17 (21.72)	0.44	4.84 (2.98)	4.82 (2.96)	135 (69)	728.11 (88.5)	53
Net. 11	Cancerous liver, HCC	19.14 (12.03)	19.92 (12.57)	33.83 (15.22)	3.37 (1.0)	61.24 (18.89)	0.44	5.91 (3.69)	5.33 (3.26)	80 (49)	577.98 (44.8)	52
Net. 12	Cancerous liver, CRC	5.49 (3.36)	6.76 (4.66)	19.84 (10.15)	4.42 (1.42)	60.47 (19.98)	0.38	3.29 (2.0)	3.7 (2.33)	491 (136)	544.79 (24.6)	66
Net. 13	Cancerous liver, CRC	6.44 (4.1)	6.26 (3.98)	23.84 (11.8)	4.59 (1.66)	55.5 (20.63)	0.32	3.99 (2.45)	3.72 (2.32)	427 (222)	463.76 (18.0)	54
Net. 14	Cancerous liver, EC	12.45 (7.55)	10.92 (6.73)	48.51 (22.53)	3.64 (1.27)	45.1 (16.13)	0.29	5.23 (3.18)	4.22 (2.58)	287 (192)	476.94 (68.8)	45
Net. 15	Cancerous liver, CRC	13.54 (8.5)	11.23 (6.97)	44.38 (19.67)	3.05 (1.13)	50.68 (21.07)	0.32	3.97 (2.46)	3.44 (2.09)	740 (292)	418.45 (36.6)	52

Cancer patients: data and analysis. Finally, we tested our simulation-informed parameter estimation on dMRI scans of 13 patients suffering from advanced solid tumours (7 females, 5 males), who participated in an ongoing imaging study at the Vall d'Hebron Institute of Oncology (Barcelona, Spain). Patients were scanned on the same 1.5T Siemens Avanto system used to acquire data on healthy volunteers, and according to the same imaging protocol. dMRI scans underwent the same processing as described above, obtaining voxel-wise maps of v_m, v_s, ANB, f_V and D^*. Mean and standard deviation of such metrics within tumours were obtained, with tumours manually segmented by an expert radiologist (R.P.L.). The estimated vascular signal was plotted as a function of the b-value in illustrative cancer ROIs.

3. Results

3.1. Vascular networks

Fig. 2 illustrates the 15 vascular networks generated in this study from liver tumour biopsies. Out of the total, 3 were segmented on non-cancerous liver parenchyma, while the remaining 12 on cancerous tissue. The 3 non-cancerous networks were drawn on liver tissue found on the histological slide, adjacent to tumour tissue (n = 2 melanoma metastases; n = 1 ovarian cancer metastasis). The 12 networks drawn on cancerous tissue came from primary liver hepatocellular carcinoma (HCC, n = 5), or from liver metastases of colorectal cancer (CRC, n = 5), endometrial cancer (n = 1), and melanoma (n = 1).

Table 1 reports salient statistics of the vascular networks shown in Fig. 2, related to capillary radii, length, velocity distribution, number of vascular segments sensed by flowing spins and number of input/output paths. None of the networks contain close loops, and all capillary segments are always part of at least one flow path connecting the inlet to the outlet. The network size varies from approximately 240 to up to 600 µm. The number of segments varies from 42 to 77, while the mean input/output path length from approximately 316 to 753 µm. The table shows that different network morphologies lead to different blood velocity distributions. For example, mean v_m across VFR realisations can vary from as low as approximately 4 mm/s up to 25 mm/s. This range of variation is mirrored in the average number of capillaries blood travels through during the simulation (ANB metric), which varies from just over 12 up to almost 57 segments (note that in some cases, ANB can be slightly higher than the total number of segments, given that spins reaching the outlet of the network continue flowing in a copy of the network itself). The mean path length PL_m also varies considerably, e.g., from just over 300 µm for network 3, exhibiting the fastest flow among networks, to up to roughly 700 µm, as in networks 5 or 6. Notably, networks characterised by longer PL_m tend to feature slower flows — a finding consistent with the fact that longer input/output paths are characterised by higher flow resistance for a fixed path radius (see Eq. (2)). Supplementary Fig. 2 shows distributions of v_m, v_s and ANB for all networks, across the 10 different inlet/outlet realisations and given an illustrative input VFR $q_{in} = 3.1 \cdot 10^{-3}$ mm³/s. Distributions are skewed, and strong contrasts in terms of v_m, v_s and ANB are seen across networks (e.g., compare Net 3 with Net 4). Supplementary Fig. 3 shows correlation coefficients among all possible pairs of metrics. There is a strong, positive correlation between v_m and v_s and ANB (0.89, 0.82), and a moderate positive correlation between v_s and ANB (0.55). All of v_m, v_s and ANB are negatively correlated with L_m, r_m and PL_m (strongest correlations between ANB and r_m, of −0.93; weakest for v_s and L, of −0.19). Finally, L_m and PL_m are positively correlated with r_m (correlation of 0.68 and 0.44). VFR and velocity are positively correlated (e.g., correlation of 0.47 between v_m and q_s).

Supplementary Fig. 4 shows scatter plots of mean VFR, mean velocity, mean radius and path length along input/output flow paths (q_p, v_p,

r_p and PL), for all 54 271 paths contained in our networks. There is a positive, weak Spearman's correlation between q_p and r_p (0.24), and a moderate negative correlation between v_p and r_p (−0.53). A moderate, positive correlation between q_p and v_p (0.58) and between r_p and PL (0.34) is also seen. Notably, the plots contain large clouds of points that visually contain several sub-clusters, each with distinctive slopes and offsets in the scatter plane.

Fig. 3 shows examples of VFR and blood velocity fields reconstructed in two vascular networks with SpinFlowSim, alongside dMRI signals. The two networks were segmented on non-cancerous liver parenchyma of a patient suffering of melanoma (top panel, Net 6) and on metastatic CRC (bottom panel, Net 12). The figure highlights that distributions of VFRs and velocities arise across network segments, owing to their different resistance to flow. The segments with the highest VFRs do not necessarily feature the highest velocities, due to differences in terms of segment diameter. The VFR distributions lead to fast dMRI signal attenuation in both networks, with most of the signal decayed by $b = 150$ s/mm^2. The signal decay is not mono-exponential (note the log-scale in the y-axis). Oscillatory patterns are also seen as well as some diffusion time dependence, with the dMRI signal decreasing slightly with increasing Δ at fixed b.

Supplementary Figs. 5 and 6 show vascular signals from one realisation of all vascular networks for increasing diffusion times (Δ of 10, 100 and 1000 ms; $\delta = 0.5$ ms; $q_{in} = 3.1 \cdot 10^{-3}$ mm^3/s). Signals were obtained by averaging measurements from 2 (Supplementary Fig. 5) and 32 (Supplementary Fig. 6) directions. The signals exhibit oscillations as a function of the b-value. On visual inspections, the oscillation increase when Δ increases from 10 to 100 ms, and then decrease for Δ of 1000 ms, especially when signals are obtained by averaging over 32 directions (supplementary Fig. 6). When averaging is performed over only 2 orthogonal directions (Supplementary Fig. 5), there are examples of networks where the number of oscillations is largest for Δ of 1000 ms (e.g., networks 7, 9, 11), and several more cases where the number of oscillations is similar across Δ (e.g., 4, 5, 12, 14). These residual signal fluctuations are seen for very high levels of signal attenuation (i.e., 10^{-2} to 10^{-3}), and are likely driven by directional biases. Averaging over a rich set of directions, in general, reduces signal oscillations (Supplementary Figs. 6 and 7).

3.2. Microvascular property estimation from dMRI

3.2.1. In silico estimation

Fig. 4 reports results from *in silico* estimation of v_m, v_s and ANB from noisy vascular signals, synthesised according to protocols "TRSE", "PGSE", "richPGSE" and "richPGSEsubset". There is a moderate to strong correlation between ground truth and estimated v_m, v_s and ANB values for protocols "PGSEinvivo" and "TRSEinvivo" (minimum Pearson's correlation: 0.41 for v_s for protocol "TRSE"; maximum correlation of 0.79 for ANB for protocol "PGSEinvivo"). Correlation is instead strong for protocol "richPGSE" and, to a lesser extent, for the protocol "richPGSEsubset", derived from it. We observe, for example, a Pearson's correlation of 0.81 and 0.73 for metric ANB, estimated respectively from protocol "richPGSE" and "richPGSEsubset". As an example, Supplementary Fig. 8 illustrates the complete set of synthetic signals generated for protocol "TRSEinvivo" and "PGSEinvivo" across the 15 segmented networks. The figure highlights that the signal decay spans several orders of magnitude: variations in the microvascular characteristics of the networks lead to remarkably different vascular dMRI signals. In Supplementary Fig. 8, a small number of networks exhibits considerably less signal decay than other networks – for example, Networks 4, 8 and 10. As apparent from Table 1, these feature among the highest mean capillary length L_m and mean path length PL_m, and among the lowest mean velocity v_m.

3.2.2. In vivo estimation

Fig. 5 shows the estimated vascular signal in different ROIs of one healthy volunteer per MRI scanner. Some of the features seen in synthetic signals can also be observed in *in vivo* measurements, as for example: a trend towards signal decrease with increasing diffusion time, seen in the spleen and liver ROIs (protocol "TRSEinvivo"); oscillations as a function of the b-value, as in the spleen and in the kidney cortex ROIs (protocol "PGSEinvivo"). Signal oscillations in the liver are instead compatible with fluctuations at the noise floor level.

Fig. 6 shows IVIM metrics f_V and D^* alongside v_m, v_s and ANB in the liver and spleen of healthy volunteer 1 (1.5T scanner). On visual inspection, f_V and D^* are systematically higher in the liver than in the spleen. This contrast is mirrored by v_m, v_s and ANB, which are as well higher in the former organ than in the latter. Fig. 7 reports the same maps, but for volunteer 4, scanned on the 3T system. Spatial trends agree with those observed on the 1.5T scanner. For example, the liver shows the highest f_V and v_m, while the kidney medulla exhibits higher values of all of f_V, D^*, v_m, v_s and ANB compared to the kidney cortex. Fig. 8 reports instead mean and standard errors of all metrics within several ROIs (liver, kidney medulla and cortex, and spleen), and in all healthy volunteers. Mean and standard deviation are also reported in Table 2. Inter-organ differences are seen, as for example higher D^*, v_m, v_s and ANB in the liver, compared to the spleen. Trends of inter-subject differences are also seen. E.g., in healthy volunteer 1, higher values of all of f_V, D^*, v_m, v_s and ANB in the kidney medulla than in the kidney cortex are seen. However, in healthy volunteer 2, D^* is higher in the cortex than in the medulla, and differences between medulla and cortex among all other metrics are less marked. Values of all metrics from healthy volunteer 3 are in between those from healthy volunteers 1 and 2. Those from healthy volunteer 4, scanned on the 3T system with a different protocol, are qualitatively consistent with those from the 1.5T system.

Fig. 9 shows representative microvascular maps in cancer. The figure refers to adrenal gland metastases of a patient suffering from rectal cancer (patient 8), and includes the visualisation of maps in surrounding, non-cancerous tissues, as in the liver and spleen parenchymas. Supplementary Fig. 9 shows instead the vascular dMRI signal estimated within such metastases, which exhibits a trend towards decrease as the diffusion time increases. In the adrenal tumours, both IVIM metrics f_V and D^* as well as microvascular v_m, v_s and ANB show intra-tumour contrasts. For example, we observe a core of lower f_V and D^* in both metastases. This spatial trend is mirrored by metrics v_m, v_s and ANB: the lower v_m, v_s and ANB point towards slower and less variable blood velocity in the core of the tumour, and predict blood to travel through fewer vessel segments, as compared to the outer ring. Overall, v_m, v_s and ANB exhibit similar contrasts among each other, but certain differences are also seen e.g., voxels with high v_m that do not necessarily show the highest ANB values. The metastases show low overall vascularisation, with f_V, D^*, v_m, v_s and ANB all lower than the values seen in the liver, being more comparable to values seen in the spleen.

Table 3 reports patient demographics and mean and standard deviation of all vascular metrics within tumours. The metrics highlight inter-tumour differences in terms of dMRI-derived vascularisation metrics. For example, breast cancer metastases feature the highest vascular signal fraction f_V among all tumours. Conversely, the highest D^* is seen in a lung cancer adrenal gland metastasis (patient 11), which also features the highest v_m, v_s and ANB across the whole cohort. The lowest D^* is instead seen in liver metastasis of rectal cancer (patient 8), a trend that is mirrored by v_m and ANB, which in this case are the lowest across all tumours. As compared to values reported in Table 2, tumours appear less vascularised than the liver, featuring a lower f_V. Capillary flow in the tumours also appears slower than in the liver but faster, for example, than in the spleen. For example, D^*, v_m, v_s and ANB vary in ranges that are qualitatively comparable to those seen for the kidney medulla on the healthy volunteers.

Table 2

Summary of healthy volunteers' demographics (age in years, sex) and trends of microvascular metrics f_V, D^*, v_m, v_s and ANB within the manually-segmented ROIs (mean and standard deviation). For sex, F indicated female, while M male. For the acquisition on the 1.5T system, routine IVIM metrics f_V and D^* were obtained at fixed diffusion time, on the dMRI scan with the shortest TE.

Scanner	Volunteer	ROI	v_m [mm/s]	v_s [mm/s]	ANB [segments]	f_v	D^* [µm²/ms]
1.5T (TRSE)	1 (M, 35)	Liver	14.95 (8.39)	16.5 (7.94)	55.0 (39.66)	0.42 (0.17)	23.79 (31.1)
		Kidney medulla	9.59 (5.82)	10.99 (6.69)	30.05 (24.13)	0.65 (0.16)	12.88 (4.3)
		Kidney cortex	5.99 (1.65)	5.95 (1.68)	13.42 (3.91)	0.53 (0.04)	8.3 (0.97)
		Spleen	7.09 (8.64)	8.88 (10.34)	46.09 (63.39)	0.09 (0.06)	22.89 (32.19)
	2 (F, 34)	Liver	14.74 (8.37)	16.14 (8.23)	54.3 (40.75)	0.25 (0.11)	18.78 (19.92)
		Kidney medulla	8.25 (8.98)	9.16 (9.7)	26.68 (30.07)	0.28 (0.21)	7.46 (5.73)
		Kidney cortex	6.95 (5.69)	7.88 (7.13)	21.79 (18.06)	0.24 (0.09)	9.97 (4.1)
		Spleen	8.24 (6.39)	10.27 (8.07)	26.62 (18.61)	0.12 (0.05)	7.54 (3.39)
	3 (M, 25)	Liver	11.24 (8.23)	13.64 (8.9)	47.72 (49.67)	0.37 (0.19)	16.52 (14.41)
		Kidney medulla	10.77 (7.95)	12.51 (8.73)	44.41 (46.23)	0.48 (0.18)	18.45 (26.38)
		Kidney cortex	4.34 (2.57)	5.09 (2.99)	14.97 (7.77)	0.25 (0.07)	9.27 (4.11)
		Spleen	6.28 (5.47)	7.98 (5.9)	22.94 (21.2)	0.14 (0.07)	15.89 (23.7)
3T (PGSE)	4 (M, 32)	Liver	12.12 (8.46)	15.72 (9.24)	43.64 (33.28)	0.45 (0.16)	16.67 (21.05)
		Kidney medulla	9.81 (6.41)	12.73 (7.95)	30.12 (23.61)	0.62 (0.16)	15.91 (14.32)
		Kidney cortex	5.67 (3.47)	7.71 (4.61)	17.91 (10.65)	0.45 (0.08)	8.07 (2.13)
		Spleen	4.31 (3.63)	6.12 (5.47)	15.81 (9.33)	0.28 (0.1)	7.01 (3.21)

Table 3

Summary of patients' demographics and key clinical data (primary cancer type, location of the imaged tumours, patients' sex and age, in years) and trends of microvascular metrics f_V, D^*, v_m, v_s and ANB within the manually-segmented tumours (mean and standard deviation). For sex, F indicated female, while M male. Routine IVIM metrics f_V and D^* were obtained at fixed diffusion time, on the dMRI scan with the shortest TE.

ID	Primary cancer	Tumour(s) location	Sex	Age	v_m [mm/s]	v_s [mm/s]	ANB [segments]	f_V	D^* [µm²/ms]
Pat. 1	Endometrial	Uterus	F	65	7.34 (8.11)	8.41 (8.38)	28.86 (37.71)	0.11 (0.12)	14.44 (22.35)
Pat. 2	Melanoma	Liver	F	84	7.12 (9.14)	7.76 (8.71)	31.45 (43.12)	0.20 (0.24)	27.16 (43.33)
Pat. 3	Gastric	Soft tissues	M	62	7.78 (8.90)	8.53 (8.71)	34.88 (46.89)	0.09 (0.09)	21.09 (35.53)
Pat. 4	Melanoma	Liver, lung, pleura	F	61	10.72 (9.21)	11.97 (9.23)	42.24 (45.49)	0.19 (0.17)	24.05 (33.60)
Pat. 5	Melanoma	Liver	M	76	9.96 (8.05)	11.26 (7.93)	39.84 (41.39)	0.04 (0.14)	19.62 (21.99)
Pat. 6	Lung	Liver	M	55	5.76 (8.33)	6.64 (8.26)	26.88 (40.85)	0.14 (0.13)	15.51 (30.47)
Pat. 7	Gastric	Stomach	F	68	5.80 (7.27)	7.10 (7.52)	24.76 (28.91)	0.25 (0.18)	13.62 (22.17)
Pat. 8	Rectal	Adrenal glands	M	61	4.80 (7.14)	5.78 (7.58)	20.80 (32.32)	0.27 (0.18)	10.13 (20.32)
Pat. 9	Gastric	Liver	F	70	7.49 (8.43)	8.69 (8.51)	31.35 (40.54)	0.22 (0.18)	20.58 (35.76)
Pat. 10	Colon	Liver	F	48	6.77 (8.05)	7.86 (8.21)	28.21 (38.83)	0.22 (0.15)	17.50 (30.04)
Pat. 11	Lung	Adrenal glands	M	62	13.37 (9.42)	15.15 (9.85)	55.18 (52.69)	0.26 (0.15)	34.10 (44.59)
Pat. 12	Breast	Liver	F	33	11.15 (10.75)	11.94 (10.48)	54.71 (60.86)	0.39 (0.24)	14.40 (27.20)
Pat. 13	Lung	Adrenal glands	M	78	7.77 (8.75)	8.88 (8.97)	32.96 (44.13)	0.15 (0.13)	22.85 (36.79)

Supplementary Fig. 10 reports Spearman's correlation coefficients between all possible pairs of vascular metrics, as obtained across the 13 cancer patients. IVIM D^* is significantly, positively correlated with all of v_m, v_s and ANB ($r_s = 0.55$, $p = 0.049$ with v_m; $r_s = 0.57$, $p = 0.044$ with v_s; $r_s = 0.64$, $p = 0.019$ with ANB). No significant correlations are instead seen between f_V and any of v_m, v_s and ANB. D^* and f_V are weakly, negatively correlated between each other ($r_s = -0.25$, $p = 0.394$).

4. Discussion

4.1. Summary and key findings

This work presents SpinFlowSim, an open-source simulator of blood flow based on pipe network analysis. The simulation framework, tailored for the laminar flow regime at the micro-capillary level, enables the synthesis of DW signals for any desired input dMRI gradient waveform. We demonstrate SpinFlowSim on 15 microvascular networks, reconstructed from biopsies in a variety of liver cancers and in non-cancerous liver parenchyma. These allowed us to simulate micro-perfusion IVIM signals for realistic dMRI protocols, in the low b regime. The signals exhibit complex, non-mono-exponential behaviour, pointing towards the co-existence of spin pools experiencing different flow regimes, compatible with signal patterns observed *in vivo*. The simulation of synthetic signals paired with corresponding sets of microvascular characteristics enabled the practical estimation of these properties from any input dMRI measurement set, given simulations of the corresponding acquisition protocol. We showcase the approach *in silico* and on *in vivo* scans of healthy volunteers and cancer patients, obtaining patterns of microvascular metrics that are plausible given known anatomy and cancer pathophysiology.

4.2. Simulation framework

Our simulator relies on a well-established computational approach for laminar flow characterisation in capillaries. This links the pressure drop across a capillary to the VFR passing through it, via a flow resistance proportionality factor (Schmid et al., 2015; Van et al., 2021). In this study, as a first proof-of-concept, we borrowed an empirical expression for this resistance from Blinder et al. (2013), and used the freely available *PySpice* (Salvaire, 2023) package to convert the VFR estimation problem into the analysis of a passive electric circuit. Our strategy, computationally efficient, retrieves the VFR distribution across all segments of a vascular network. These are used to estimate the mean blood velocity in each capillary and, finally, the trajectories of flowing spins, by numerical integration of the velocity field over time. By superimposing arbitrary dMRI gradient wave forms to spins flowing in networks reconstructed from histology, our framework enables the synthesis of realistic IVIM signals, without making assumptions on the specific flow regime in which measurements take place (e.g., diffusive/ballistic Kennan et al., 1994; Scott et al., 2021). Our approach offers a practical way to characterise the salient characteristics of micro-capillary perfusion, and its relationship to dMRI. It may therefore play a key role in the development of innovative dMRI methods for vascular characterisation with unprecedented specificity to physiology, urgently needed for non-invasive cancer characterisation.

4.3. Vascular networks

We studied HE and CD31-stained histological images from liver tumour biopsies, obtained from cancer patients suffering from advanced solid tumours. From these data, we manually reconstructed 15

2D vascular networks, on which we simulated blood flow by varying the input VFR and the inlet/outlet positions. We characterised the networks in terms of the underlying blood velocity distribution (v_m and v_s parameters), and by introducing a metric quantifying the average number of capillary branches spins flow through, referred to as ANB. Overall, our simulations generated a total of 1500 network realisations, which provide insight into microvascular blood perfusion.

The most important observation is that the networks exhibit blood velocity and VFR distributions, sizes, number of segments, number of input/output paths, characteristic path and segment lengths, and ANB values that can vary considerably from each other. For example, the mean velocity v_m ranges from approximately 4 to 25 mm/s. The wide variation of microperfusion metrics is exemplified, for example, by Net 11 and 12 in Table 1, which feature a mean v_m of 19 and 5 mm/s, despite exhibiting a similar mean capillary length of circa 60 μm. This finding suggests that, for the typical diffusion times that can be probed in clinical settings (15–65 ms approximately), spins in the vascular compartment likely experience flow regimes that can vary considerably from subject to subject. On the one hand, this implies that hypothesising a specific regime in IVIM modelling (e.g., diffusive versus ballistic Kennan et al., 1994; Scott et al., 2021), may not suffice to capture the full complexity of blood micro-perfusion in real-world cohorts. On the other hand, these trends suggest that multiple descriptors may be required to characterise in full the topology of a vascular network. For example, networks featuring larger sizes do not necessarily feature more segments (e.g., network 5 vs. 8), showing that non-trivial relationships between different network parameters exist. These results motivate the development of novel microperfusion dMRI methods, which attempt to retrieve network features with higher biologically specificity than traditional IVIM metrics such as D^*.

Our simulations also suggest that remarkably different patterns of vascular dMRI signals are to be expected, even for short, clinically-feasible IVIM dMRI protocols, as exemplified by two examples in Fig. 3. Our simulated signals exhibit complex patterns as a function of the b-value and the diffusion time, e.g., fast decay, typical of the diffusive regime, as well as oscillatory behaviours, as instead expected in the ballistic regime (note that the PGSE signal for a set of uniformly distributed straight capillaries, characterised by the same blood velocity v, is $s = sinc(\gamma v G \delta \Delta)$ Scott et al., 2021). Moreover, they also feature a clearly non-mono-exponential behaviour as a function of b, pointing again towards the co-existence of different flowing spin pools within the same network, potentially characterised by different flow regimes. Some of the oscillations can be explained by unaccounted directional biases of our networks, given that averaging over two directions may not suffice to fully compensate for the directional dependence of the signal, especially when the decay is strong (Supplementary Figs. 5, 6 and 7). This implies that our synthetic signals may be slightly exaggerating complex features compared to what could be observed *in vivo*. Nevertheless, our pilot analysis suffices to demonstrate that numerical approaches such as SpinFlowSim may lead to more accurate characterisation of unexplored properties ofvascular dMRI signals — e.g., concerning flow anisotropy or apparent pseudo-diffusion and kurtosis tensors, as illustrated in Supplementary Fig. 11 for the apparent pseudo-diffusion tensor in an exemplificative case —, ultimately opening up new opportunities for the development of more specific biomarkers of micro-perfusion.

4.4. Microvascular property estimation

We also investigated whether it is possible to use the synthetic signals generated through SpinFlowsim to inform the non-invasive estimation of microvascular properties. For this purpose, we interpolated the full set of paired synthetic signals and microvascular parameters, obtaining numerical forward models that can be fitted through standard NNLS approaches. We specifically investigated the feasibility of estimating v_m, v_s and ANB.

Firstly, we studied v_m, v_s and ANB estimation on noisy *in silico* signals. We considered 4 protocols: two matched those of available *in vivo* dMRI scans, and were based on DW TRSE and standard PGSE (protocols "TRSEinvivo" and "PGSEinvivo"). An additional PGSE protocol ("richPGSE") implemented a very rich acquisition, sampling several b-values as well as diffusion times, while the fourth protocol was a subset of the rich acquisition ("richPGSEsubset"). All protocols point towards the feasibility of estimating v_m, v_s and ANB: we observed strong correlations between ground truth and estimated v_m and ANB, and moderate correlations for v_s. As expected, performances were the highest for the richest protocol, with correlations as high as 0.81 for the ANB metric, yet still acceptable for the shorter protocols (e.g., correlation of 0.63 for ANB and the TRSEinvivo protocol and of 0.80 for PGSEinvivo, which features more b-values than TRSEinvivo). These promising results, obtained without requiring any explicit analytical modelling of the signal, highlight the potential utility of simulation-informed microvascular property estimation, motivating its testing *in vivo*.

Following *in silico* experiments, we moved on and tested whether v_m, v_s and ANB can also be estimated *in vivo*. For this purpose, we analysed dMRI scans acquired according to two dMRI protocols on four healthy volunteers and in 13 cancer patients. We estimated vascular dMRI signals and visualised them in different ROIs, observing complex signal features that are compatible with those observed in synthetic signals. These included, for example, signal oscillations as a function of b in areas such as the spleen, suggestive of low capillary velocity and ballistic flow regime, or diffusion time dependence. These complex signal behaviours, which cannot be captured in full with simple mono-exponential functions of the form e^{-bD^*}, justify the investigation of advanced models of the dMRI vascular signal. To this end, we fitted v_m, v_s and ANB alongside standard IVIM f_V and D^*, and assessed trends qualitatively in several organs in the healthy volunteers, and in the patients' tumours.

In healthy volunteers, all metrics show high level of variability on visual inspection, which is confirmed by cross-organ trends in Fig. 8. The variability, qualitatively comparable between f_V/D^* and v_m, v_s and ANB, is in line with the well-known challenge of estimating microvascular property accurately with dMRI (Barbieri et al., 2020). This finding suggests that more robust parameter estimation procedures may be needed than those used here (e.g., Bayesian fitting or deep learning Barbieri et al., 2016a, 2020), for the effective deployment of simulation-informed fitting in clinical settings. However, despite the variability, metrics show trends that are compatible with known physiology, and are consistent across two MRI scanners, which use different field strengths (1.5T and 3T) and different diffusion encoding strategies. For example, in healthy volunteers the liver shows much higher f_V, D^*, v_m, v_s and ANB than in the spleen. This finding is plausible considering that the liver is a highly vascularised organ, a blood reservoir receiving approximately 25% of the cardiac output, despite representing only 2.5% of the body weight (Lautt, 2010). We also observe higher v_m, v_s and ANB in the kidney medulla than in the cortex, a finding that may be reflecting their different vascularisation. Regarding kidneys, we do not observe a clear trend in terms of cortex-medulla differences in standard IVIM f_V and D^* (e.g., f_V is higher in the medulla than in the cortex for both healthy volunteers, while D^* is in one case higher, and in the other lower). This is in line with recent studies, which have found high variability and strong inter-subject/inter-machine differences of kidney IVIM (Barbieri et al., 2016a; Ljimani et al., 2018; Stabinska et al., 2023).

Finally, we also demonstrated the feasibility of simulation-informed microvascular quantification in a pilot cohort of 13 cancer patients suffering from advanced solid tumours. While this demonstration only represents a first, exploratory proof-of-concept, it serves to highlight that contrasts seen in v_m, v_s and ANB are physiologically plausible, and consistent with patterns seen on f_V and D^*. For example, reduced v_m, v_s and ANB is seen in areas of low f_V and D^* compatible with

reduced perfusion, expected in the tumour core (Karsch-Bluman et al., 2019; Herman et al., 2011), exemplified by Fig. 9. *In vivo*, v_m, v_s and ANB are positively correlated among each other, and they correlate moderately to strongly to IVIM D^*. These correlations agree with the correlations observed in simulations (compare Supplementary Fig. 3 and Supplementary Fig. 10), and may indicate that v_m, v_s and ANB, while providing complementary information to each other, are sensitive to similar characteristics of the network morphology. For example, the strong correlation between v_m and v_s, indicating that higher variability in blood velocity has to be expected as the mean velocity increases, may be a signature of heteroscedasticity of the blood velocity distribution across capillaries.

All in all, our *in vivo* results demonstrate the feasibility of simulation-informed microvascular mapping in dMRI. While further confirmation and more detailed metric characterisation is required in future studies, realistic flow simulations informed by histology may increase the accuracy of dMRI microvascular signal models. Ultimately, these may provide innovative, biologically-specific indices of microperfusion, urgently sought for the non-invasive evaluation of cancer neo-angiogenesis, vascular heterogeneity and in treatment during the design of anti-angiogenic drugs.

4.5. Potential applications of simulation-informed microvasculature mapping

Potential applications of the technique span both cancer diagnosis/detection as well as monitoring, once a cancer is found. For example, the characterisation of liver tumours that cannot be biopsied is still an unsolved issue in radiology. The non-invasive characterisation of tumour vascularity could provide unique information to radiologists for the differential diagnosis of infiltrative hepatocellular carcinoma from other conditions, such as intrahepatic cholangiocarcinoma or other liver diseases, e.g., fibrosis, steatosis or other vascular disorders (Vernuccio et al., 2021; Wang et al., 2022). Regarding monitoring, SpinFlowSim-based parameter estimation may provide useful descriptors of cancer microvasculature in the context of antiangiogenic treatments.

In essence, the applications of SpinFlowSim microvasculature mapping are similar to those typically envisioned for more common IVIM, with the major difference that SpinFlowSim is designed to boost the biological specificity of the voxel-wise metrics towards capillary microperfusion. As opposed to standard IVIM-like approaches, our simulation-informed framework can account for the exact gradient timings used in the acquisition, and thus implicitly deal with diffusion-time dependence and with flow regime transitions, notoriously difficult to model analytically. This has the potential of delivering metrics that are directly related to the underlying dynamical processes of microvascular perfusion in tissues, mitigating scanner-dependent or protocol-dependent biases, unlike less specific IVIM D^* or related metrics.

4.6. Methodological considerations and limitations

In this article, we show the potential utility of flow simulations to inform dMRI signal modelling and analysis. We provide a first demonstration, based on a simplified simulation framework as a preliminary proof-of-concept. For example, we rely on an empirical expression for the resistance to flow across a capillary, borrowed from a model of cortical perfusion in the mouse primary sensory cortex (Blinder et al., 2013). While this model accounts for salient features of blood flow resistance in capillaries (e.g., the effect of an average hematocrit and erythrocyte-wall interactions), a more realistic characterisation of the capillary resistance would be obtained by accounting for the Fåhræus-Lindqvist's, the Fåhræus' and the phase separation effects (Schmid et al., 2015; Van et al., 2021). This would have required the simulation of the propagation of actual erythrocytes through the network, until a steady-state is reached, so that a per-capillary hematocrit (and hence,

effective blood viscosity) can be calculated. Here we did not simulate erythrocyte propagation, being this computationally demanding. Nevertheless, we acknowledge that it would enable more realistic representations of flow patterns within micro-capillary networks. We plan to include erythrocyte flow in future work, and also extend SpinFlowSim to account, for example, for oscillatory pressure patterns and vessel deformation, and for fluid exchange between capillaries and the interstitial space. Another possible development is related to the simulation of *open* networks, i.e., networks that are not fully contained within a synthetic voxel. In its current version, SpinFlowSim enables the simulations of such networks by discarding specific, undesired spin trajectories, for instance by thresholding spin positions (see Supplementary Fig. 12 for an example). Nevertheless, we acknowledge that further optimisation of the toolbox is required to allow for a more agile simulation of these cases.

Furthermore, we acknowledge that for this first demonstration, we simulated vascular dMRI signals only on 2D capillary networks. While SpinFlowSim is designed to work with generic 3D networks, here we focussed on 2D representations due to the availability of 2D data (i.e., HE and CD31-stained biopsies). We accounted for this by averaging synthetic dMRI signals generated for two, orthogonal, in-plane gradient directions. However, in future we plan to increase the fidelity of our flow simulations by reconstructing 3D networks.

Related to the point above, the vascular networks reconstructed from histology for this article were obtained at the capillary level. Therefore, our synthetic signals may not be representative of larger vessels, including smaller feeding arterioles and small veins or venules. This implies that maps of v_m, v_s and ANB from our approach has to be taken with care in presence of larger vessels. In future, we plan to expand our vascular signal dictionary to include realisations of larger vessels, and thus improve the generalisability of our simulation-informed fitting.

We also acknowledge that the overall size of our networks is smaller than that of actual capillary beds that are contained in *in vivo* dMRI voxels, as these would be at least one order of magnitude larger. This may introduce correlations among spin trajectories that would be otherwise blurred in the case of flow through more intricate, disordered, and larger networks. For the same reason, the inter-network variability observed in this study is likely to overestimate the true *in vivo* biological variability, where vascular networks are larger and hence likely more homogeneous. Exploratory analysis of data from Table 1 reveals a moderate-to-strong correlation between the standard deviation of ANB and the network size (Spearman's correlation of -0.667, $p = 0.0067$), while only a weak correlation between the standard deviation of v_m and v_s with the network size (Spearman's correlation of -0.220, $p = 0.432$ and of 0.072, $p = 0.780$ respectively). This finding suggests that the apparent variability of at least some of our metrics, as well as the amount of signal oscillations, could be reduced if larger networks were to be considered. In future work, we plan to increase the realism of our numerical dMRI models by incorporating additional vascular characteristics so far neglected, e.g., larger and more complex capillary branches; networks that are not fully contained within a voxel; or presence of feeding arterioles and output venules, as also mentioned above. All of these can significantly alter the network topology and its VFR patterns, resulting in considerable changes of the vascular dMRI signals, as illustrated in two exemplificative cases in Supplementary Fig. 12 and Supplementary Fig. 13.

Regarding the practical simulation of spin trajectories, we point out that for realistic input VFR and network topologies, some of the flowing spins reach the outlet before the simulation has been finalised. In general, we did not find an obvious solution on how to best deal with such spins. For example, in related work (Van et al., 2021), these would be discarded for the computation of the dMRI signal. In this first implementation, we decided to send such spins through a copy of the network whose inlet had been shifted and made coincide exactly with the original network outlet. This ensures that even those parts of

the network that are close to the outlet contribute to the dMRI signal for a considerable portion of the simulation. Examples of the effect of this condition on spin trajectories are shown in Supplementary Video 1 and Supplementary Video 2, showing flow through two networks over 72 ms of simulation, in which respectively 2.62% and 23.04% of the spins are sent to the network copy. While this design allows for full conservation of mass during the simulation, we acknowledge that it may also exaggerate correlations among spins. In future work we plan to compare systematically different approaches to deal with spins reaching the network output and, more generally, with comparable vascular simulation engines (Van et al., 2021; Lashgari et al., 2025).

As far as the correlation among properties of our synthetic networks are concerned instead, we acknowledge that some of the reported correlations require further explanation, e.g., the negative correlation between r_m and v_m, which at a first glance does not appear to match Eq. (2). This finding has to be interpreted by noting that the VFR or velocity through a capillary segment are related to the overall resistance of the local network element to which the segment belongs. In other words, a 1:1 relationship $v \propto r^2$ (or $q \propto r^4$) from Eqs. (1), (2) and (3) can only be expected when comparing capillary segments that receive the same input flow and that are arranged in parallel: two capillaries with radii $r_2 > r_1$ and same length L, arranged in series, would feature $v_2 < v_1$, since it must hold that $q_1 = q_2$. The fact that when a negative correlation between mean velocity and mean radius along all flow paths is seen in Supplementary Fig. 4, points towards a potential higher predominance of serial configurations, rather than parallel. Notably, in Supplementary Fig. 4 not even the set of VFRs q_p and blood velocities v_p along flow paths are perfectly correlated, despite being the condition $q(x, y, z) = \frac{v(x,y,z)}{\pi r(x,y,z)^2}$ met *exactly* in each point (x, y, z) of a capillary. These findings highlight that different proportionality factors among pairs of flow metrics can exist when comparing different flow paths, implying that both positive or negative correlations may be observed, depending on the network topology.

Another point to acknowledge is that in this study we focussed on the characterisation of vascular dMRI signals, and devised a simulation-informed fitting procedure requiring pure vascular signals as input. For this reason, the analysis of *in vivo* signals required disentangling vascular from extra-vascular tissue signals, since low b measurements include contributions from both. This was achieved by extrapolating an ADC fit performed on b-values with negligible vascular signal contribution, and thus required identifying a b-value threshold. An approach of this type, i.e., splitting the vascular-tissue signal characterisation in two steps, is sometimes referred to as *segmented IVIM fitting* (Gurney-Champion et al., 2018; Wang et al., 2021). While segmented fitting reduces the variability of vascular metrics, since it avoids the challenging, joint estimation of vascular and tissue properties (Barbieri et al., 2020), it may lead to biases in f_V estimates, since f_V may depend, at least slightly, on the b-value threshold. In future, we plan to improve the simulation-informed fitting performed here, by employing more advanced estimation techniques for the joint computation of vascular and tissue properties.

Regarding the vascular signal measurement *in vivo*, we point out that our acquisitions featured 3 orthogonal gradient directions. Similarly to what was discussed for *in silico* signals, we acknowledge that such a reduced scheme may not suffice to fully resolve the directional dependence of the vascular signal. Richer acquisitions schemes would be required to characterise in full the complexity of vascular measurements *in vivo*, e.g., through the computation of apparent vascular tensors (Notohamiprodjo et al., 2015; Hilbert et al., 2016; Voorter et al., 2025).

Lastly, we acknowledge that the results reported here should be confirmed by future studies. These would require the acquisition of data from additional healthy volunteers and from larger patient cohorts, and should include diffusion images from different MRI scanners and from more advanced dMRI protocols. Here, in patients, we used a simple acquisition scheme in the low b regime ($b = 0$ and $b =$

$\{50, 100\}$ s/mm^2 at 3 diffusion times; protocol "TRSEinvivo"). However, the accurate characterisation of the complex signal patterns arising from microvasculature, require denser b samplings, e.g., to capture oscillatory patterns as a function of b. In this article, we included a healthy volunteer scan featuring a richer b-value protocol in the [0; 100] s/mm^2 range (protocol "PGSEinvivo"), demonstrating oscillatory signal patterns *in vivo* in organs such as the spleen. Moreover, results from *in silico* experiments show that this protocol allows for a better estimation of the microvascular parameters v_m, v_s and ANB, compared to the protocol "TRSEinvivo". These findings highlight the importance of the design of b-value sampling scheme for accurate microvascular parameter estimation in cancer patients *in vivo*. Similarly, higher image quality and increased sensitivity to micro-perfusion could also be achieved, for example, by improving the robustness of the dMRI acquisition with cardiac/respiratory gating, or by employing flow-compensated (Wetscherek et al., 2015) gradient wave forms, or advanced b-tensor encoding (Nilsson et al., 2021).

5. Conclusions

SpinFlowSim, our open-source, freely-available python simulator of blood micro-perfusion in capillaries, enables the synthesis and characterisation of realistic microvascular dMRI signals. Perfusion simulations in vascular networks reconstructed from histology may inform the non-invasive, numerical estimation of innovative microvascular properties through dMRI, whose feasibility is demonstrated herein *in vivo* in healthy subjects and in cancer patients.

CRediT authorship contribution statement

Anna Kira Voronova: Writing – review & editing, Writing – original draft, Visualization, Validation, Software, Resources, Project administration, Methodology, Investigation, Formal analysis, Data curation, Conceptualization. **Athanasios Grigoriou:** Writing – review & editing, Software, Resources, Methodology, Data curation. **Kinga Bernatowicz:** Writing – review & editing, Project administration, Investigation, Data curation. **Sara Simonetti:** Writing – review & editing, Investigation. **Garazi Serna:** Writing – review & editing, Investigation, Data curation. **Núria Roson:** Writing – review & editing, Resources. **Manuel Escobar:** Writing – review & editing, Resources. **Maria Vieito:** Writing – review & editing, Investigation. **Paolo Nuciforo:** Writing – review & editing, Resources, Project administration, Funding acquisition, Data curation. **Rodrigo Toledo:** Writing – review & editing, Resources, Project administration, Funding acquisition, Data curation. **Elena Garralda:** Writing – review & editing, Resources, Project administration, Funding acquisition, Data curation. **Els Fieremans:** Writing – review & editing, Supervision, Methodology, Conceptualization. **Dmitry S. Novikov:** Writing – review & editing, Supervision, Methodology, Conceptualization. **Marco Palombo:** Writing – review & editing, Supervision, Methodology, Conceptualization. **Raquel Perez-Lopez:** Writing – review & editing, Resources, Project administration, Methodology, Funding acquisition, Data curation, Conceptualization. **Francesco Grussu:** Writing – review & editing, Writing – original draft, Visualization, Validation, Supervision, Software, Resources, Project administration, Methodology, Investigation, Funding acquisition, Formal analysis, Data curation, Conceptualization.

Declaration of competing interest

Acknowledgements

Appendix A. Supplementary data

Supplementary material related to this article can be found online at https://doi.org/10.1016/j.media.2025.103531.

Data availability

SpinFlowSim is made freely available as a GitHub repository at the permanent address: https://github.com/radiomicsgroup/SpinFlowSim. The repository includes the 15 vascular networks presented in this study that can be used to generate synthetic vascular signals for simulation-informed model fitting. The code for simulation-informed fitting is freely available as part of *BodyMRITools* at the address: https://github.com/fragrussu/bodymritools (script *mri2micro_dictml.py*). Raw *in vivo* human MRI scans cannot be made freely available at this stage due to ethical restrictions.

References

Andersson, J.L., Skare, S., Ashburner, J., 2003. How to correct susceptibility distortions in spin-echo echo-planar images: application to diffusion tensor imaging. Neuroimage 20 (2), 870–888.

Barbieri, S., Donati, O.F., Froehlich, J.M., Thoeny, H.C., 2016a. Comparison of intravoxel incoherent motion parameters across MR imagers and field strengths: evaluation in upper abdominal organs. Radiol. 279 (3), 784–794, Publisher: Radiological Society of North America.

Barbieri, S., Donati, O.F., Froehlich, J.M., Thoeny, H.C., 2016b. Impact of the calculation algorithm on biexponential fitting of diffusion-weighted MRI in upper abdominal organs. Magn. Reson. Med. 75 (5), 2175–2184, Publisher: Wiley Online Library.

Barbieri, S., Gurney-Champion, O.J., Klaassen, R., Thoeny, H.C., 2020. Deep learning how to fit an intravoxel incoherent motion model to diffusion-weighted MRI. Magn. Reson. Med. 83 (1), 312–321. http://dx.doi.org/10.1002/mrm.27910.

Blinder, P., Tsai, P.S., Kaufhold, J.P., Knutsen, P.M., Suhl, H., Kleinfeld, D., 2013. The cortical angiome: an interconnected vascular network with noncolumnar patterns of blood flow. Nature Neurosci. 16 (7), 889–897. http://dx.doi.org/10.1038/nn.3426.

Buizza, G., Paganelli, C., Ballati, F., Sacco, S., Preda, L., Iannalfi, A., Alexander, D.C., Baroni, G., Palombo, M., 2021. Improving the characterization of meningioma microstructure in proton therapy from conventional apparent diffusion coefficient measurements using Monte Carlo simulations of diffusion MRI. Med. Phys. 48 (3), 1250–1261, Publisher: Wiley Online Library.

Dappa, E., Elger, T., Hasenburg, A., Düber, C., Battista, M.J., Hötker, A.M., 2017. The value of advanced MRI techniques in the assessment of cervical cancer: a review. Insights Into Imaging 8, 471–481, Publisher: Springer.

Fieremans, E., Lee, H.-H., 2018. Physical and numerical phantoms for the validation of brain microstructural MRI: A cookbook. NeuroImage 182, 39–61. http://dx.doi.org/10.1016/j.neuroimage.2018.06.046.

Fokkinga, E., Hernandez-Tamames, J.A., Ianus, A., Nilsson, M., Tax, C.M., Perez-Lopez, R., Grussu, F., 2024. Advanced diffusion-weighted MRI for cancer microstructure assessment in body imaging, and its relationship with histology. J. Magn. Reson. Imaging 60, 1278–1304. http://dx.doi.org/10.1002/jmri.29144.

Ginsburger, K., Matuschke, F., Poupon, F., Mangin, J.-F., Axer, M., Poupon, C., 2019. MEDUSA: A GPU-based tool to create realistic phantoms of the brain microstructure using tiny spheres. NeuroImage 193, 10–24, Publisher: Elsevier.

Gurney-Champion, O.J., Klaassen, R., Froeling, M., Barbieri, S., Stoker, J., Engelbrecht, M.R., Wilmink, J.W., Besselink, M.G., Bel, A., Van Laarhoven, H.W., et al., 2018. Comparison of six fit algorithms for the intra-voxel incoherent motion model of diffusion-weighted magnetic resonance imaging data of pancreatic cancer patients. PloS One 13 (4), e0194590.

Hall, M.G., Alexander, D.C., 2009. Convergence and parameter choice for Monte-Carlo simulations of diffusion MRI. IEEE Trans. Med. Imaging 28 (9), 1354–1364, Publisher: IEEE.

Herman, A.B., Savage, V.M., West, G.B., 2011. A quantitative theory of solid tumor growth, metabolic rate and vascularization. PloS One 6 (9), e22973.

Hilbert, F., Bock, M., Neubauer, H., Veldhoen, S., Wech, T., Bley, T.A., Köstler, H., 2016. An intravoxel oriented flow model for diffusion-weighted imaging of the kidney. NMR Biomed. 29 (10), 1403–1413.

Huinen, Z.R., Huijbers, E.J., van Beijnum, J.R., Nowak-Sliwinska, P., Griffioen, A.W., 2021. Anti-angiogenic agents—overcoming tumour endothelial cell anergy and improving immunotherapy outcomes. Nat. Rev. Clin. Oncol. 18 (8), 527–540, Publisher: Nature Publishing Group UK London.

Iima, M., Kataoka, M., Kanao, S., Onishi, N., Kawai, M., Ohashi, A., Sakaguchi, R., Toi, M., Togashi, K., 2018. Intravoxel incoherent motion and quantitative non-Gaussian diffusion MR imaging: evaluation of the diagnostic and prognostic value of several markers of malignant and benign breast lesions. Radiol. 287 (2), 432–441, Publisher: Radiological Society of North America.

Ivanov, K., Kalinina, M., Levkovich, Y.I., 1981. Blood flow velocity in capillaries of brain and muscles and its physiological significance. Microvasc. Res. 22 (2), 143–155.

Jayson, G.C., Kerbel, R., Ellis, L.M., Harris, A.L., 2016. Antiangiogenic therapy in oncology: current status and future directions. Lancet 388 (10043), 518–529, Publisher: Elsevier.

Karsch-Bluman, A., Feiglin, A., Arbib, E., Stern, T., Shoval, H., Schwob, O., Berger, M., Benny, O., 2019. Tissue necrosis and its role in cancer progression. Oncogene 38 (11), 1920–1935.

Kellner, E., Dhital, B., Kiselev, V.G., Reisert, M., 2016. Gibbs-ringing artifact removal based on local subvoxel-shifts. Magn. Reson. Med. 76 (5), 1574–1581. http://dx.doi.org/10.1002/mrm.26054.

Kennan, R.P., Gao, J.-H., Zhong, J., Gore, J.C., 1994. A general model of microcirculatory blood flow effects in gradient sensitized MRI. Med. Phys. 21 (4), 539–545.

Késmárky, G., Kenyeres, P., Rábai, M., Tóth, K., 2008. Plasma viscosity: a forgotten variable. Clin. Hemorheol. Microcirc. 39 (1), 243–246, Publisher: IOS Press.

Kiselev, V.G., 2017. Fundamentals of diffusion MRI physics. NMR Biomed. 30 (3), e3602.

Lashgari, M., Yang, Z., Bernabeu, M.O., Li, J.-R., Frangi, A.F., 2025. SpinDoctor-IVIM: A virtual imaging framework for intravoxel incoherent motion MRI. Med. Image Anal. 99, 103369. http://dx.doi.org/10.1016/j.media.2024.103369.

Lautt, W.W., 2010. Hepatic circulation: physiology and pathophysiology. http://dx.doi.org/10.4199/C00004ED1V01Y200910ISP001.

Le Bihan, D., 2019. What can we see with IVIM MRI? Neuroimage 187, 56–67, Publisher: Elsevier.

Le Bihan, D., Breton, E., Lallemand, D., Grenier, P., Cabanis, E., Laval-Jeantet, M., 1986. MR imaging of intravoxel incoherent motions: application to diffusion and perfusion in neurologic disorders. Radiol. 161 (2), 401–407. http://dx.doi.org/10.1148/radiology.161.2.3763909.

Le Bihan, D., Turner, R., 1992-09. The capillary network: a link between IVIM and classical perfusion. Magn. Reson. Med. 27 (1), 171–178. http://dx.doi.org/10.1002/mrm.1910270116.

Lee, H.-H., Fieremans, E., Novikov, D.S., 2021. Realistic microstructure simulator (RMS): Monte Carlo simulations of diffusion in three-dimensional cell segmentations of microscopy images. J. Neurosci. Methods 350, 109018, Publisher: Elsevier.

Ljimani, A., Lanzman, R.S., Müller-Lutz, A., Antoch, G., Wittsack, H.-J., 2018. Nongaussian diffusion evaluation of the human kidney by Padé exponent model. J. Magn. Reson. Imaging 47 (1), 160–167.

Morelli, L., Palombo, M., Buizza, G., Riva, G., Pella, A., Fontana, G., Imparato, S., Iannalfi, A., Orlandi, E., Paganelli, C., Baroni, G., 2023. Microstructural parameters from DW-MRI for tumour characterization and local recurrence prediction in particle therapy of skull-base chordoma. Med. Phys. Publisher: Wiley Online Library.

Munn, L.L., 2003. Aberrant vascular architecture in tumors and its importance in drug-based therapies. Drug Discov. Today 8 (9), 396–403, Publisher: Elsevier.

Nedjati-Gilani, G.L., Schneider, T., Hall, M.G., Cawley, N., Hill, I., Ciccarelli, O., Drobnjak, I., Wheeler-Kingshott, C.A.G., Alexander, D.C., 2017. Machine learning based compartment models with permeability for white matter microstructure imaging. NeuroImage 150, 119–135, Publisher: Elsevier.

Nguyen, H., Li, J., Grebenkov, D., Le Bihan, D., Poupon, C., 2014. Parameters estimation from the diffusion MRI signal using a macroscopic model. In: Journal of Physics: Conference Series. Vol. 490, IOP Publishing, 012117.

Nilsson, M., Alerstam, E., Wirestam, R., Ståhlberg, F., Brockstedt, S., Lätt, J., 2010. Evaluating the accuracy and precision of a two-compartment Kärger model using Monte Carlo simulations. J. Magn. Reson. 206 (1), 59–67, Publisher: Elsevier.

Nilsson, M., Eklund, G., Szczepankiewicz, F., Skorpil, M., Bryskhe, K., Westin, C.-F., Lindh, C., Blomqvist, L., Jäderling, F., 2021. Mapping prostatic microscopic anisotropy using linear and spherical b-tensor encoding: a preliminary study. Magn. Reson. Med. 86 (4), 2025–2033.

Notohamiprodjo, M., Chandarana, H., Mikheev, A., Rusinek, H., Grinstead, J., Feiweier, T., Raya, J.G., Lee, V.S., Sigmund, E.E., 2015. Combined intravoxel incoherent motion and diffusion tensor imaging of renal diffusion and flow anisotropy. Magn. Reson. Med. 73 (4), 1526–1532.

Palombo, M., Alexander, D.C., Zhang, H., 2019. A generative model of realistic brain cells with application to numerical simulation of the diffusion-weighted MR signal. NeuroImage 188, 391–402, Publisher: Elsevier.

Panagiotaki, E., Schneider, T., Siow, B., Hall, M.G., Lythgoe, M.F., Alexander, D.C., 2012. Compartment models of the diffusion MR signal in brain white matter: a taxonomy and comparison. NeuroImage 59 (3), 2241–2254. http://dx.doi.org/10.1016/j.neuroimage.2011.09.081.

Peixoto, T.P., 2023. Descriptive vs. Inferential Community Detection in Networks: pitfalls, Myths and Half-Truths. Cambridge University Press, http://dx.doi.org/10.1017/9781009118897.

Perucho, J.A.U., Wang, M., Vardhanabhuti, V., Tse, K.Y., Chan, K.K.L., Lee, E.Y.P., 2021. Association between IVIM parameters and treatment response in locally advanced squamous cell cervical cancer treated by chemoradiotherapy. Eur. Radiol. 1–10, Publisher: Springer.

Pries, A.R., Secomb, T.W., 2008. Blood flow in microvascular networks. In: Microcirculation. Elsevier, pp. 3–36.

Rafael-Patino, J., Romascano, D., Ramirez-Manzanares, A., Canales-Rodríguez, E.J., Girard, G., Thiran, J.-P., 2020. Robust Monte-Carlo simulations in diffusion-MRI: Effect of the substrate complexity and parameter choice on the reproducibility of results. Front. Neuroinformatics 14, 8, Publisher: Frontiers Media SA.

Salvaire, F., 2023. PySpice. URL: https://pyspice.fabrice-salvaire.fr.

Schmid, F., Reichold, J., Weber, B., Jenny, P., 2015. The impact of capillary dilation on the distribution of red blood cells in artificial networks. Am. J. Physiol.- Hear. Circ. Physiol. 308 (7), H733–H742. http://dx.doi.org/10.1152/ajpheart.00335.2014.

Scott, L.A., Dickie, B.R., Rawson, S.D., Coutts, G., Burnett, T.L., Allan, S.M., Parker, G.J., Parkes, L.M., 2021. Characterisation of microvessel blood velocity and segment length in the brain using multi-diffusion-time diffusion-weighted MRI. J. Cereb. Blood Flow Metab. 41 (8), 1939–1953.

Stabinska, J., Zöllner, H.J., Thiel, T.A., Wittsack, H.-J., Ljimani, A., 2023. Image downsampling expedited adaptive least-squares (IDEAL) fitting improves intravoxel incoherent motion (IVIM) analysis in the human kidney. Magn. Reson. Med. 89 (3), 1055–1067.

Van, V.P., Schmid, F., Spinner, G., Kozerke, S., Federau, C., 2021. Simulation of intravoxel incoherent perfusion signal using a realistic capillary network of a mouse brain. NMR Biomed. 34 (7), e4528. http://dx.doi.org/10.1002/nbm.4528.

Veraart, J., Novikov, D.S., Christiaens, D., Ades-Aron, B., Sijbers, J., Fieremans, E., 2016. Denoising of diffusion MRI using random matrix theory. NeuroImage 142, 394–406. http://dx.doi.org/10.1016/j.neuroimage.2016.08.016.

Vernuccio, F., Porrello, G., Cannella, R., Vernuccio, L., Midiri, M., Giannitrapani, L., Soresi, M., Brancatelli, G., 2021. Benign and malignant mimickers of infiltrative hepatocellular carcinoma: tips and tricks for differential diagnosis on CT and MRI. Clin. Imaging 70, 33–45.

Voorter, P.H., Jansen, J.F., van der Thiel, M.M., van Dinther, M., Postma, A.A., van Oostenbrugge, R.J., Gurney-Champion, O.J., Drenthen, G.S., Backes, W.H., 2025. Diffusion-derived intravoxel-incoherent motion anisotropy relates to CSF and blood flow. Magn. Reson. Med. 93 (3), 930–941. http://dx.doi.org/10.1002/mrm.30294.

Voronova, A., Grigoriou, A., Bernatowicz, K., Simonetti, S., Serna, G., Roson, N., Escobar, M., Vieito, M., Nuciforo, P., Toledo, R., Garralda, E., Sala-Llonch, R., Fieremans, E., Novikov, D.S., Palombo, M., Perez-Lopez, R., Grussu, F., 2024a. SpinFlowSim: a blood flow simulation framework for histology-informed diffusion MRI microvasculature mapping in cancer. MedRxiv http://dx.doi.org/10.1101/2024.07.15.24310335, arXiv:https://www.medrxiv.org/content/early/2024/07/15/2024.07.15.24310335.full.pdf, URL: https://www.medrxiv.org/content/early/2024/07/15/2024.07.15.24310335.

Voronova, A., Grigoriou, A., Bernatowicz, K., Simonetti, S., Serna, G., Roson, N., Escobar, M., Vieito, M., Nuciforo, P., Toledo, R., Garralda, E., Sala-Llonch, R., Palombo, M., Perez-Lopez, R., Grussu, F., 2024b. FlowSim : a blood flow simulator for histology-informed diffusion mri micro-vasculature mapping in cancer. In: Proceedings of the International Society for Magnetic Resonance in Medicine. ISMRM, ISMRM, p. 0586.

Wang, X., Song, J., Zhou, S., Lu, Y., Lin, W., Koh, T.S., Hou, Z., Yan, Z., 2021. A comparative study of methods for determining intravoxel incoherent motion parameters in cervix cancer. Cancer Imaging 21, 1–11.

Wang, X., Wang, S., Yin, X., Zheng, Y., 2022. MRI-based radiomics distinguish different pathological types of hepatocellular carcinoma. Comput. Biol. Med. 141, 105058.

Weine, J., McGrath, C., Dirix, P., Buoso, S., Kozerke, S., 2024. CMRsim–a python package for cardiovascular MR simulations incorporating complex motion and flow. Magn. Reson. Med. 91 (6), 2621–2637. http://dx.doi.org/10.1002/mrm.30010, Publisher: Wiley Online Library.

Wetscherek, A., Stieltjes, B., Laun, F.B., 2015. Flow-compensated intravoxel incoherent motion diffusion imaging. Magn. Reson. Med. 74 (2), 410–419.

Wu, D., Zhang, J., 2019. Evidence of the diffusion time dependence of intravoxel incoherent motion in the brain. Magn. Reson. Med. 82 (6), 2225–2235, Publisher: Wiley Online Library.

Zheng, T., Yan, G., Li, H., Zheng, W., Shi, W., Zhang, Y., Ye, C., Wu, D., 2023. A microstructure estimation transformer inspired by sparse representation for diffusion MRI. Med. Image Anal. 86, 102788.

Anna Kira Voronova is a predoctoral scientist at the Vall d'Hebron Institute of Oncology (VHIO), which she joined in 2022, and PhD student at the University of Barcelona (Spain). With a background in biomedical engineering, her research focuses on the design of realistic blood flow simulations to inform biophysical models in MRI,

e.g., for Intravoxel Incoherent Motion (IVIM) imaging approaches. Her ultimate goal is the development of novel non-invasive biomarkers of microvascular perfusion to aid cancer detection and therapy evaluation.

Athanasios Grigoriou is a predoctoral scientist and PhD student at the Vall d'Hebron Institute of Oncology (VHIO), with a background in mechanical engineering and aeronautics. He is currently pursuing a PhD in Biomedicine, at the University of Barcelona (Spain). His main research interests focus on computational diffusion Magnetic Resonance Imaging (dMRI) methods for cancer microstructure characterisation, based on Monte Carlo diffusion simulations.

Kinga Bernatowicz studied engineering at Gdańsk University of Technology (Poland) and later received her M.Sc. in Nuclear Engineering and Ph.D. in Physics from ETH Zurich, in Switzerland. Later she moved to Belgium, at the Paul Scherrer Institute and to the Catholic University of Leuven, to work on respiratory-motion-adapted imaging for proton therapy in cancer. She then moved to the Vall d'Hebron Institute of Oncology of Barcelona to work on Radiomics, where she was awarded an MSCA-COFUND grant to focus on investigating tumour heterogeneity using imaging habitats techniques, to predict response to immunotherapy. She has recently moved to AstraZeneca to work on biomarker development.

Dr Sara Simonetti is an investigative pathologist at the VHIO Molecular Oncology Group and at the Vall d'Hebron University Hospital of Barcelona. Her work focuses on the assessment of histological data for clinical trials and for research projects, with a focus on breast, prostate and colorectal cancer. She provides support to several research projects at VHIO.

Garazi Serna is a postdoctoral researcher in the Molecular Oncology Group at the Vall d'Hebron Institute of Oncology (VHIO) in Barcelona. Her research focuses on advanced cancer diagnostics based on histopathology, and on integrating histology data with other sources of information through artificial intelligence, in order to improve cancer diagnosis and characterisation. Examples of projects include the development of predictive models for patient responses to anti-HER2 treatment based on histological images. Additionally, Garazi Serna has worked on projects studying the persistence of Fusobacterium nucleatum in colorectal cancer and the development of multiplex IHC/RNAscope techniques for precision oncology.

Núria Roson is a research associate in the Molecular Medical Imaging group at the Vall d'Hebron Institute of Research (VHIR), and Senior Radiologist at the Vall d'Hebron University Hospital of Barcelona. Her research focusses on clinical applications of advanced imaging techniques, as for example the automation of radiological assessments through machine learning and artificial intelligence. She also supports the design and imaging protocols in several clinical studies across the Vall d'Hebron Radiology department.

Manuel Escobar is a principal researcher in the Molecular Medical Imaging group at the Vall d'Hebron Institute of Research, and head of the Radiology department at the Vall d'Hebron University Hospital in Barcelona. His work focusses on nuclear medicine, computed tomography and magnetic resonance imaging. He aims to develop innovative non-invasive readouts based on imaging capable of improve the sensitivity of clinical radiology in the diagnostic process, but also the accuracy of follow-up patient monitoring. He is involved in significant translational research projects such as X4HPC, PHASE IV AI, and the SGR project.

Maria Vieito is an oncologist and clinical researcher specialised in investigative oncology at the Vall d'Hebron Institute of Oncology (VHIO) and the Vall d'Hebron University Hospital in Barcelona. She is involved in clinical research focused on improving cancer treatments and patient outcomes. She also plays a key role in several research projects focussing on biomarker discovery, and provides continued support for patient recruitment and monitoring in clinical trials at the Vall d'Hebron University Hospital.

Paolo Nuciforo is the Principal Investigator of the Molecular Oncology Group at the Vall d'Hebron Institute of Oncology (VHIO). The group is a core facility at VHIO, providing high-throughput support to projects requiring the acquisition or analysis of histology data. He also leads independent lines of research, e.g., focussing on the development of predictive models for response assessment based on histology, particularly in HER2-positive breast cancer, with state-of-the-art multiple immunohistochemistry.

Rodrigo Toledo, PhD MBA, is a Principal Investigator at the Vall d'Hebron Institute of Oncology (VHIO), where he leads the Biomarkers and Clonal Dynamics Group. He has extensive experience in oncology and translational research, and is specialised on the analysis of cancer genetic material found on liquid biopsies. Toledo has published over 50 research papers in high-impact scientific journals. Among his awards, the Miguel Servet Fellowship and the Swiss Bridge Foundation Award stand out.

Dr. Elena Garralda is an established researcher and oncologist at the Vall d'Hebron Institute of Oncology (VHIO) and the Vall d'Hebron Institute of Research (VHIR). She is the Principal Investigator of the Early Clinical Drug Development Group at VHIO and serves as the Director of the Research Unit for Molecular Therapy of Cancer (UITM) – CaixaResearch. Her work focuses on early-phase clinical trials and the development of new cancer therapies, including immunotherapy and targeted treatments.

Els Fieremans is an Associate Professor in the Department of Radiology at NYU Grossman School of Medicine and co-director of the MRI Biophysics group. She holds a master's degree in Engineering and Physics and a PhD in Biomedical Engineering from Ghent University, Belgium. Her research focuses on using MRI - especially diffusion imaging - to measure tissue microstructure in vivo. Her projects focus on developing new imaging markers for neurodegenerative diseases and other conditions by leveraging quantitative methods through biophysical modelling. She is specialised in biophysical simulations based on numerical phantoms, and has experience in preclinical animal imaging. She has supervised more than 10 students among Master's and PhD, and has received numerous awards, as the International Society for Magnetic Resonance in Medicine (ISMRM) Fellowship in 2024.

Dmitry S. Novikov is an Associate Professor in the Department of Radiology at NYU Grossman School of Medicine. He holds a PhD from the Massachusetts Institute of Technology and has completed postdoctoral training at Princeton and Yale Universities. Prof Novikov's research involves using analytical and numerical models to interpret cellular-level tissue structure changes measured non-invasively with diffusion and relaxation MRI. His work focuses on MRI measurements of diffusion, transverse relaxation, and perfusion to identify quantitative disease biomarkers in neurodegenerative diseases, tumours, and myopathies. He has supervised Master's, PhD and post-doctoral students (> 15 projects), since 2024 he is a Fellow of the prestigious International Society for Magnetic Resonance in Medicine (ISMRM).

Marco Palombo is a UKRI Future Leaders Fellow and Associate Professor (Senior Lecturer) in microstructure imaging at Cardiff University. He works both in the Cardiff University Brain Research Imaging Centre (CUBRIC), Cardiff (UK), where he co-leads the MicroTeam group, and in the School of Computer Science and Informatics, where he co-leads the Medical Image Computing group. A trained physicist with a solid background in biophysics, his work currently sits at the interface of machine learning, computational modelling and radiology. After graduating in physics at La Sapienza University in Rome, he worked in diffusion-weighted magnetic resonance spectroscopy in Pris (Institut d'Imagerie Biomédicale) and on brain diffusion imaging at University College London (UK), before moving to Cardiff.

Raquel Perez-Lopez is the Principal Investigator of the Radiomics Group at the Vall d'Hebron Institute of Oncology. A trained radiologist specialised on oncological imaging, she holds a PhD from the University of Barcelona. She further specialised at the Royal Marsden Hospital and the Institute of Cancer Research in London, before founding the Radiomics Group. Her research focuses on developing non-invasive imaging biomarkers to improve cancer patient care. Her main interests are the automated processing of standard-of-care imaging powered by Artificial Intelligence, and the use of whole-body diffusion-weighted MRI for prostate cancer bone metastasis characterisation. She has published in prestigious journals such as Radiology, Cell Reports Medicine and Cancer Discovery, and the impact made by her research has been featured in several TV programs at Catalan and Spanish level.

Francesco Grussu holds a biomedical engineering degree and a PhD in Magnetic Resonance Physics. He joined the Vall d'Hebron Institute of Oncology (VHIO) in 2020, where he currently works as a senior investigator in quantitative MRI development for precision oncology. He obtained BEng degree from University of Cagliari (Italy) and an MEng degree from University of Genoa (Italy), Italy, a PhD from University College London (UK) in 2016. At VHIO, he develops diffusion MRI techniques inspired by histology to improve cancer diagnosis and monitoring. At VHIO he obtained competitive grants, as a Beatriu de Pinós Fellowship and a "la Caixa" Foundation Junior Leader Fellowship in 2022.